CHARACTERIZATION OF JUNCTION PARAMETERS IN N-TYPE $FeSi_2$/P-TYPE Si HETEROJUNCTIONS

PHONGSAPHAK SITTIMART

A THESIS SUBMITTED IN PARTIAL FULFILLMENT
OF THE REQUIRMENT FOR THE DEGREE OF MASTER OF SCIENCE
IN APPLIED PHYSICS
DEPARTMENT OF PHYSICS
FACULTY OF SCIENCE
KING MONGKUT'S INSTITUTE OF TECHNOLOGY LADKRABANG
ACADEMIC YEAR 2017
KMITL-2017-SC-M-030-018

Dedicate to dad, mom and brother.

Faculty of Science
King Mongkut's Institute of Technology Ladkrabang
Thesis Certification

Thesis Title	"CHARACTERIZATION OF JUNCTION PARAMETERS IN N-TYPE $FeSi_2$/P-TYPE Si HETEROJUNCTIONS"
Student Name	Mr.Phongsaphak Sittimart
Student ID	58605073
Degree	Master of Science (Applied Physics)
Department	Physics
Thesis Advisor	Asst.Prof.Dr.Nathaporn Promros

Thesis Committee	Signatures
Asst.Prof.Dr.Prathan Buranasiri Chairperson	
Dr.Witoon Yindeesuk Examiner	
Asst.Prof.Dr.Boonchoat Poasawatyanyong External Examiner	
Asst.Prof.Dr.Nathaporn Promros Thesis Advisor	

Examination Date 29th June 2017 **Time** 09.00 - 12.00 a.m.
Place Faculty of Science room 307

Approved by Faculty of Science

(Assoc.Prof.Dr. Dusanee Thanaboripat)
Dean

Date 19 July 17

Thesis	Characterization of Junction Parameters in n-Type $FeSi_2$/p-Type Si Heterojunctions
Student	Mr. Phongsaphak Sittimart
Student ID.	58605073
Degree	Master of Science
Program	Applied Physics
Academic year	2016
Thesis advisor	Asst. Prof. Dr. Nathaporn Promros

Abstract

This thesis was divided to 2 parts. In the first part, p-type Si/n-type β-$FeSi_2$ heterojunctions were formed by employing radio frequency magnetron sputtering at a temperature for substrate of 560 °C. To compute the junction parameters, the measurement of dark current density-voltage (*J-V*) was carried out at low temperatures between 20 K and 300 K. From the computation by thermionic emission (TE) theory, the ideality factor (n) values were found to be 1.71 at 300 K and 16.83 at 20 K. The barrier height (ϕ_b) values were 0.59 eV at 300 K and 0.06 eV at 20 K. Both n and ϕ_b values, which were computed by TE theory, were consistent with those computed by means of Cheung and Norde. The series resistance (R_s) values computed by means of Norde were 10.93 Ω at 300 K and 0.15 MΩ at 20 K. These figures were consistent with those computed by means of Cheung. In the second part, p-type Si/i-UNCD/a-C/n-type NC-$FeSi_2$ heterojunctions, which were formed by pulsed laser deposition as well as coaxial arc plasma deposition, were measured the dark *J-V* at different temperatures to compute the junction parameters. Based on TE theory, the n value was found to be 1.12 at 300 K. It increased to 5.44 when the temperature decreased to 80 K. The ϕ_b value was 0.69 eV at 300 K and decreased to 0.20 eV at 80 K. These values approximately equal to those computed by means of Chueng and Norde. According to the computation by means of Chueng, The R_s values were 300.88 Ω and 4.29 MΩ at 300 K and at 80 K, respectively. These were in agreement to those computed by means of Norde.

Acknowledgement

I would like to express my deepest gratitude and thanks to my supervisor, Asst. Prof. Dr. Nathaporn Promros, for his endless support, patience, encouragement and friendship throughout this thesis. It was surely never succeeded without him. Furthermore, he is my hero, who has set fire to me to think, hope and develop in my life.

I am also thankful to Asst. Prof. Dr. Boonchoat Poasawatyanyong for his excellent guidance, valuable comments and continuous support since the bachelor degree until now. Besides, he is setting a good example for me, to learn and study the ways that help elevating my life.

Many thanks are truly the members of this thesis committees, Asst. Prof. Dr. Boonchoat Poasawatyanyong, Asst. Prof. Dr. Prathan Buranasiri and Dr. Witoon yindeesuk for their valuable time, worth discussions and comments.

Expression of appreciation is sincerely sent to Prof. Dr. Tsuyoshi Yoshitake for his facilities and apparatus at Kyushu University in Japan, and everybody in Yoshitake's laboratory for their guidance in electronic instruments.

Endless love and supporting everything from my parents, auntie Chon, and brother, help me much to survive and succeed in this thesis. They always give valuable words and sentences, which always make me get accomplishing in any difficult tasks. I very sincerely appreciate them. I have been never seeing the ways that I can compensate their favors in this life or next life. I glad to be your son.

Thanks are the members of 604 and 601 rooms for their supports and relax situations that made me feel better when I was depressed.

Unlimited knowledge was provided by KMITL lecturers, who used to teach a fool like me for everything. I sincerely appreciate to them.

Last but not the least, I want to give many thanks to Ms. Pitchaya Kumbut, who always gives encouragement and friendship since we met each other for the first times until now.

Phongsaphak Sittimart

Contents

Contents (Cont.)

Contents (Cont.)

List of Tables

List of Figures

List of Figures (Cont.)

List of Figures (Cont.)

Chapter 1
Introduction

1.1 Background

Previous reports from a variety of researchers stated that iron disilicide ($FeSi_2$) in orthorhombic phase (β) has been discussed as an innovative candidate for the low-cost optoelectronic devices operating in a wavelength range of near-infrared (NIR) [1-3]. It is owning to its distinctive optical features such as a large optical absorption coefficients [4,5]. It has also been found to have an indirect energy gap of 0.74 eV, which is below the direct energy gap of 0.85 eV. These energy gaps are relevant to the wavelength ranges for the optical fiber telecommunication (between 1.3 and 1.55 μm) [6,7]. The vital feature for β-$FeSi_2$ is the possibility to form epitaxial layer on Si with 2-5% lattice mismatches [3,5,6]. It is well known that its compound consists of nontoxic Fe and Si elements that are abundant in nature [8]. Another interesting candidate is $FeSi_2$ in nanocrystalline (NC) structure that has the crystalline diameter of approximately 5 nm. It has been reported that it was found to possess the physical features nearly to β-$FeSi_2$ including $FeSi_2$ in amorphous form [9]. The interesting properties of NC-$FeSi_2$ are that it is capable to be formed on various solid substrates at room temperature. Additionally, its optical absorption coefficients is larger than that of β-$FeSi_2$ [10,11]. For these reasons, it has been discussed as a potentially innovative material for Si-based optoelectronic applications. Recently, many researchers reported the creation of heterojunction comprising Si wafer and $FeSi_2$ thin films including the application of these heterojunctions to photodiode [9-11]. However, there has been a few researches to study the estimation for their important junction parameters.

Hence, the aim for the current study is the estimation of the junction parameters for the β-$FeSi_2$/Si and NC-$FeSi_2$/ instrinsic ultrananocrystalline diamond/amorphous carbon composite (i-UNCD/a-C)/Si heterojunctions created by means of physical vapor deposition (PVD). Their junction parameters as a function of temperature were characterized and discussed in detail.

1.2 Research aims

- To form the β-$FeSi_2$/Si and NC-$FeSi_2$/i-UNCD/a-C/Si heterojunctions by PVD technique.
- To estimate the important junction parameters such as ideality factor (n), barrier height (ϕ_b), and series resistance (R_s) from the current-voltage (I-V) curves based on the Thermionic emission theory (TE), Cheung's and Norde's methods.
- To study the characteristic of the junction parameters as a function of temperature.

1.3 Scope of research

- The β-$FeSi_2$/Si and NC-$FeSi_2$/i-UNCD/a-C/Si heterojunctions were created by PVD technique.
- The vital heterojunction parameters at low temperatures were computed and analyzed by TE theory, Cheung's and Norde's methods.

1.4 Research organization

Table 1.1 Research Procedures

Procedures	Period (month)			
	May -July	Aug-Oct	Sep-Dec	Jan-Apr
Study literatures relate to the research aims	←			
Form the β-$FeSi_2$/Si and NC-$FeSi_2$/i-UNCD/a-C/Si junctions		←	→	
Measure the *I-V* characteristics at low temperatures		←	→	
Compute the junction parameter from *I-V* curves			←	→
Write the master thesis				↔

1.5 Expectation

- Expose the junction parameters of the β-$FeSi_2$/Si and NC-$FeSi_2$/i-UNCD/a-C/Si heterojunctions.
- Understand the characteristics of the junction parameters of β-$FeSi_2$/Si and NC-$FeSi_2$/i-UNCD/a-C/Si heterojunctions at low temperatures.
- Compare the junction parameters computed by TE theory with those computed by Cheung's and Norde's methods to check the consistency.

Chapter 2

Theory and Related Research

2.1 Chapter overview

This chapter presents the details of theory and related research concerning the current thesis. The author will present initially the features of β- and NC-$FeSi_2$. After that, the discussions concerning to heterojunctions will be presented in sequence. Finally, the author describes the meaning of the important junction parameters and method from several researchers in order to compute junction parameters.

2.2 β-$FeSi_2$ properties

The phase diagram of Fe-Si system is displayed in Fig. 2.1. In the Fe-Si phase diagram, there are silicide phases as follows: Fe_3Si (cubic), Fe_2Si (cubic), Fe_5Si_3 (hexagonal), ε-FeSi (cubic), β-$FeSi_2$ (orthorhombic), and α-$FeSi_2$ (tetragonal) [12].

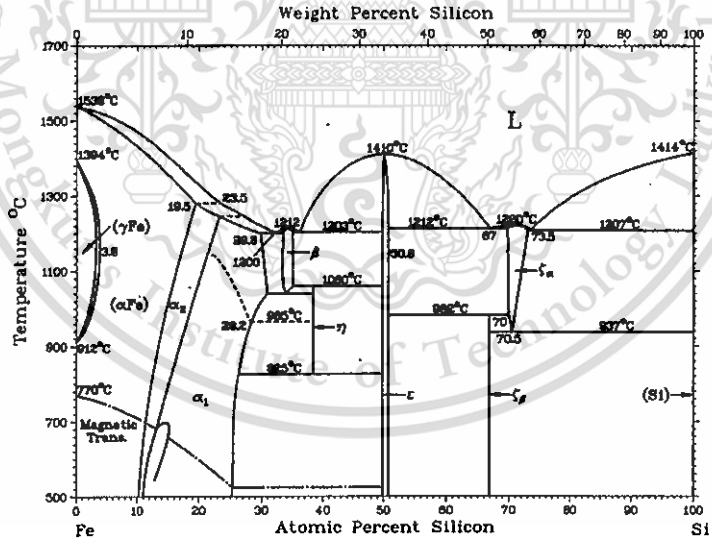

Figure 2.1 Fe-Si phase diagram [12].

For disilicide ($FeSi_2$) composition as shown in the range of atomic percent silicon between 65 and 70 in Fig. 2.1, there are 3 phases such as tetragonal α-$FeSi_2$, orthorhombic β-$FeSi_2$, and cubic γ-$FeSi_2$. The α-phase is a compound that can be grown at a high temperature. It is stable in the temperature range from 950°C to the

melting point. The β-phase is transforms into the α-phase when the temperature is more than 970 ℃ and is stable below 937 ℃. Among the disilicide phases, only orthorhombic β-$FeSi_2$ phase possesses semiconducting properties [12].

The β-$FeSi_2$ structure is shown in Fig. 2.2. Its lattice constants are a = 0.986 nm, b =0.778 nm, and c = 0.788 nm. The orthorhombic structure consists of 48 atoms in the primitive cell (Si 32 atoms and Fe 16 atoms) [14].

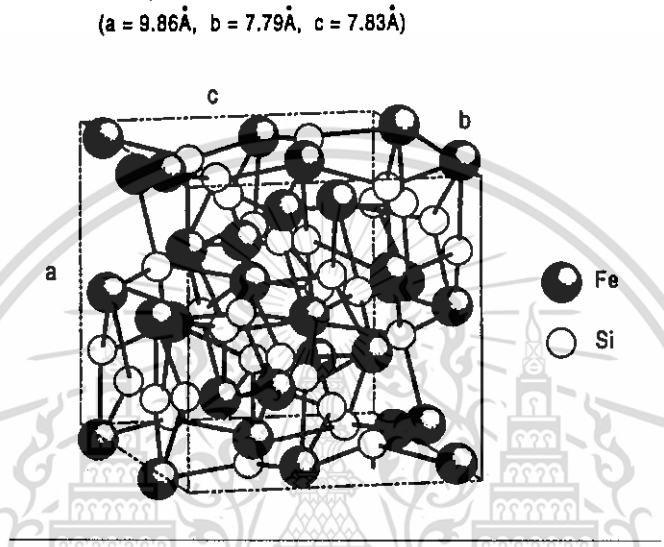

Figure 2.2 Unit cell for β-$FeSi_2$ structure [14].

Previously, T. Yoshitake, et al. [16] reported the values of direct and indirect band gap of β-$FeSi_2$. These band gaps were determined by using optical absorption spectrum of β-$FeSi_2$ layer formed utilizing facing-targets direct-current sputtering (FTDCS) as shown in Fig. 2.3. According to the results, both direct and indirect band gaps were determined approximately 0.85 and 0.75 eV, respectively, as depicted in the inset in Fig. 2.3. These determinations were consistent with those determined by M.C. Bost, et al. [4], H. Udono, et al. [17], and E. Arushanov, et al. [18].

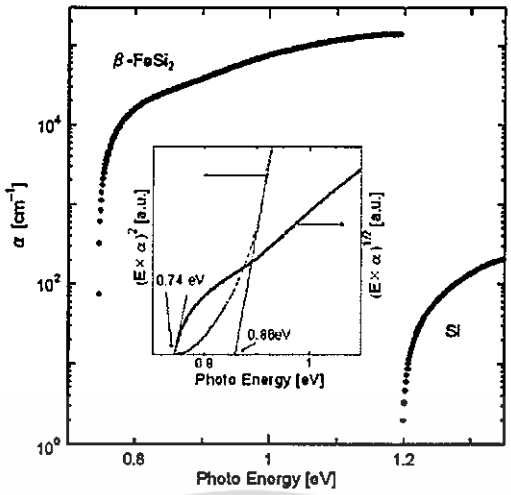

Figure 2.3 Optical absorption spectrum of β-$FeSi_2$ layer compared with the Si wafer. The inset is the plots of $(E\times\alpha)^2$ and $(E\times\alpha)^{1/2}$ versus photon energy to determine the band gaps [16].

J. E. Mahan, et al. [21] reported that the growth of β-$FeSi_2$ on Si(001) wafer had a lattices mismatch of 2.1%. They studied the epitaxial layers of β-$FeSi_2$ on Si(111) [22]. For the growth of β-$FeSi_2$ on Si(111), the heteroepitaxial relationship were $FeSi_2$(110)/Si(111) and $FeSi_2$(101)/Si(111) as depicted in Fig. 2.4 (a) and (b), respectively.

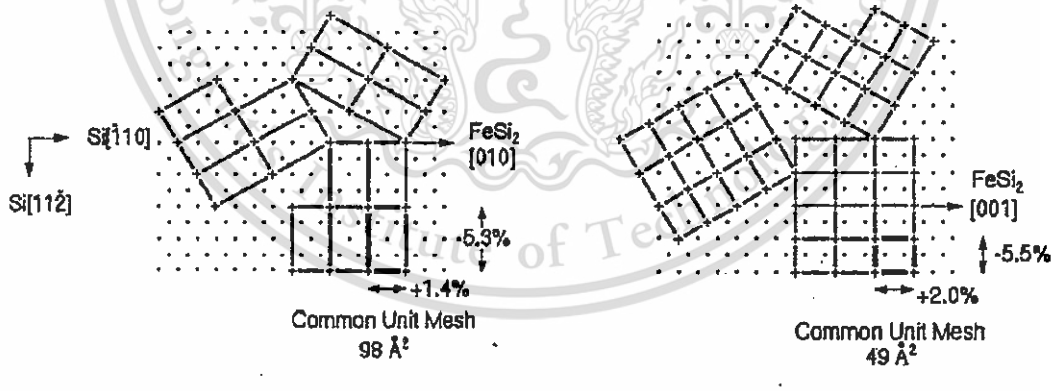

(a) (b)

Figure 2.4 Lattice matching of β-$FeSi_2$ to the Si(111) for the epitaxial relationship in the case of (a) $FeSi_2$(110)/Si(111) and (b) $FeSi_2$(101)/Si(111) [22].

Several researchers studied in epitaxial growth of β-$FeSi_2$ layer Si(111) wafer [16,23-27]. Even though there are many accomplishments in the formation of the

epitaxial growth β-$FeSi_2$ on Si(111) by several processes, these preparing processes such as molecular beam epitaxy and reactive deposition epitaxy required a post annealing at temperatures of 800 °C in order to transform phase from α to β [28]. This results in accelerating the Fe atoms to diffuse into Si sides. The diffused Fe atoms in Si potentially created a deep trap level in the Si. This could behave as a leakage center for current rectifying behavior in the junctions [29]. This is that why the heterojunctions created by such methods were not exhibited a rectifying action. Hence, the epitaxial growth of β-$FeSi_2$ on Si wafers at low temperatures should be better.

T. Yoshitake, et al. utilized facing-target direct-current sputtering (FTDCS) for epitaxial growth of β-$FeSi_2$ layer on Si(111) wafers at a substrates temperature lower than 800 °C in order to overcome such problem. They confirmed that the β-$FeSi_2$ layer formed by FTDCS was epitaxially grown on Si(111) wafer [16]. In a previous study, we achieved the epitaxial growth of β-$FeSi_2$ layer on Si(111) wafers at a substrates temperature of 560 °C by radio frequency magnetron sputtering (RFMS) [31]. According to our experimental results, we confirmed that the β-$FeSi_2$ layer were grown epitaxially on Si(111) wafer and the formed n-type β-$FeSi_2$/p-type Si heterojunctions was studied the NIR photodetection properties. Our heterojunctions showed a good rectifying action and the NIR photodetection was evidently enhanced at low temperatures as shown in Fig. 2.5.

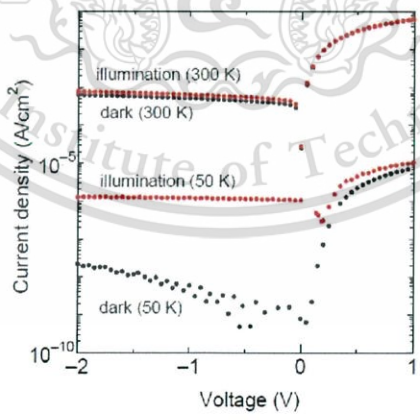

Figure 2.5 The measured dark and illuminated *J-V* at room temperature and 50 K for the heterojunctions formed by RFMS [31].

2.3 NC-$FeSi_2$ properties

T. Yoshitake, et al. accomplished in preparation of NC-$FeSi_2$ layer on Si(111) wafer by utilizing pulsed laser deposition (PLD) [34]. According to their report, NC-$FeSi_2$ layer was found to have a smooth surface. It had a crystalline diameter of approximately 5 nm, which confirmed by Dark-field TEM image as shown in Fig. 2.6. The carrier density of the films was around 10^{19} cm^{-3}, which is larger than that of β-$FeSi_2$. Moreover, they found that the NC-$FeSi_2$ layer possessed a direct optical band gap of approximately 0.87 eV, which is nearly same that reported by M. Milosavlijevic et al [32]. Besides, this value was almost equal with that of β-$FeSi_2$. K. Takarabe, et al. reported that the optical absorption coefficient of NC-$FeSi_2$ was larger than that of β-$FeSi_2$ [35]. Recently, the NC-$FeSi_2$ was utilized in application of optoelectronic devices by some research groups [9,11,36-37].

Figure 2.6 Dark-field TEM image for NC-$FeSi_2$ layer created by PLD [34].

Previously, we successfully formed n-type NC-$FeSi_2$/i-UNCD/a-C/p-type Si heterojunctions by utilizing PLD and coaxial arc plasma deposition (CAPD) [39]. The heterojunctions have been characterized the electrical properties at low temperatures. They showed a large leakage current at 300 K and it decreased at low temperatures. Also, the leakage current was reduced when compared with p-n heterojunctions created by PLD. We demonstrated that the NIR photodetection for the heterojunctions was improved at low temperatures. Figure 2.7 showed the improvement of the photocurrent for the heterojunctions at low temperatures.

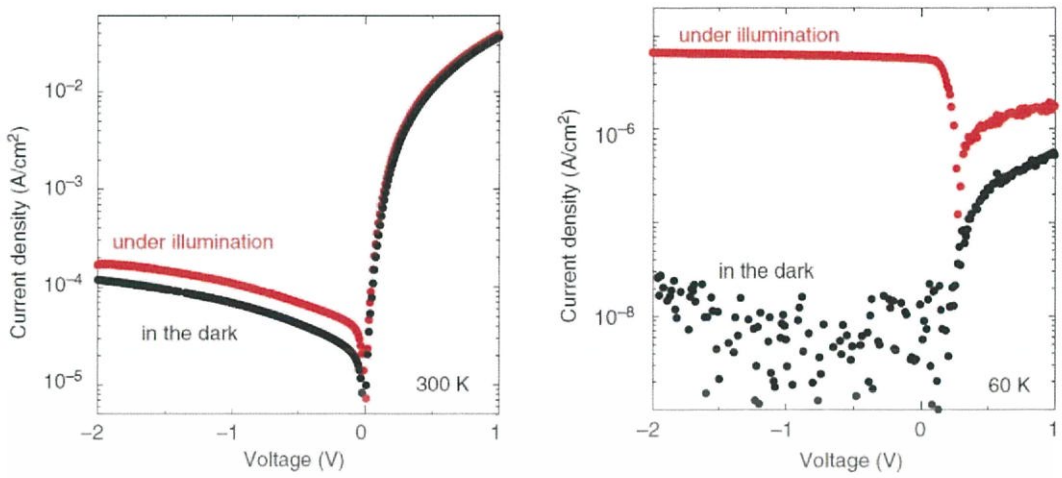

Figure 2.7 The *J-V* of heterojunctions measured in the dark and under illumination at 300 K and 60 K [39].

2.4 Heterojunctions [40-42]

A heterojunction is a formed p-n junction by two different semiconductors [40]. Heterojunction devices are more complicated than homojunctions owing to the different band gaps and electron affinities. These result in discontinues, which occur a spike in the band bending called band offset. If the spike is large enough, it acts as a barrier, which effects the current yield. There are three types of heterojunction which are shown in Fig. 2.8.

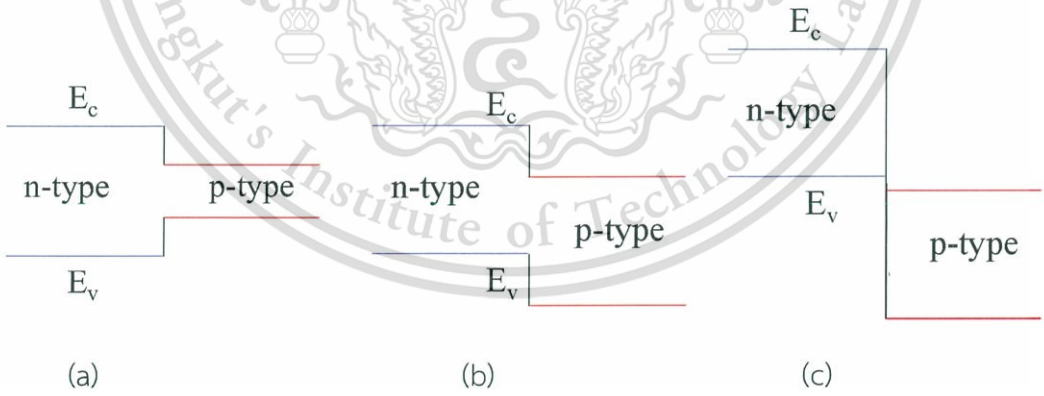

Figure 2.8 Three types of heterojunctions according to band gap alignment including (a) Type 1 (Straddling), (b) Type 2 (Staggered) and (c) Type 3 (Broken).

The transport models for heterojunctions are a development of original models for homojunctions. As seen in Fig.2.9, a spike in the band edges arises from result of different band gaps ($E_{g1,2}$), electron affinities ($\chi_{1,2}$) and work function ($\phi_{1,2}$) of two different semiconductors. The conduction band discontinuity and valance band

discontinuity can be computed by Anderson's Rule. As can be seen in Fig.2.9, the difference of electron affinities for two semiconductors gives conduction band offset,

$$\Delta E_c = \chi_2 - \chi_1 \ , \tag{2.1}$$

in the same way, the valance band discontinuity is given by

$$\Delta E_v = E_{g2} - E_{g1} - \Delta E_c = \Delta E_g - \Delta E_c \ , \tag{2.2}$$

Band offsets of the heterojunction creates extra barrier in the junction. This barrier increases the recombination of the photo-generated charges. Thus, to minimize the band offset that effects on carrier flow in a heterojunction, ΔE_c has to be minimize by choosing closer electron affinity and band gap.

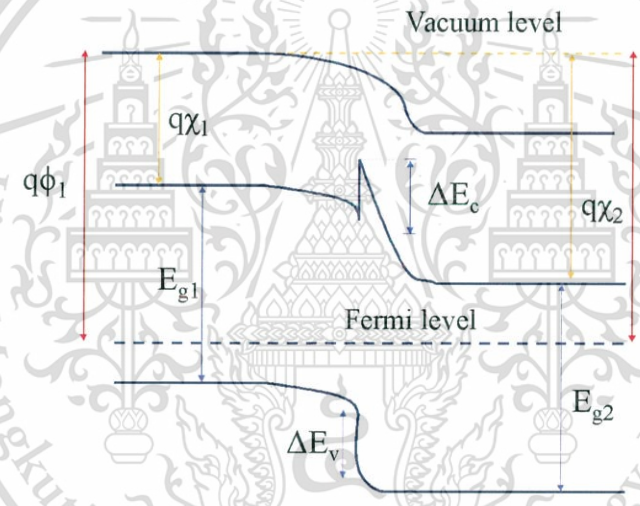

Figure 2.9 Energy band diagram of a heterojunction at thermal equilibrium condition.

Previously, M. Shaban, et al. demonstrated the energy band diagram of n-type β-$FeSi_2$/p-type Si heterojunction [41]. The electron affinity and band gap of β-$FeSi_2$ were 3.86 eV and 0.85 eV, respectively. The electron affinity and band gap of Si were 4.05 eV and 1.12 eV, respectively [41-42]. From these values, the estimation of valance band offset of β-$FeSi_2$/Si heterojunction is depicted as shown in Fig. 2.10.

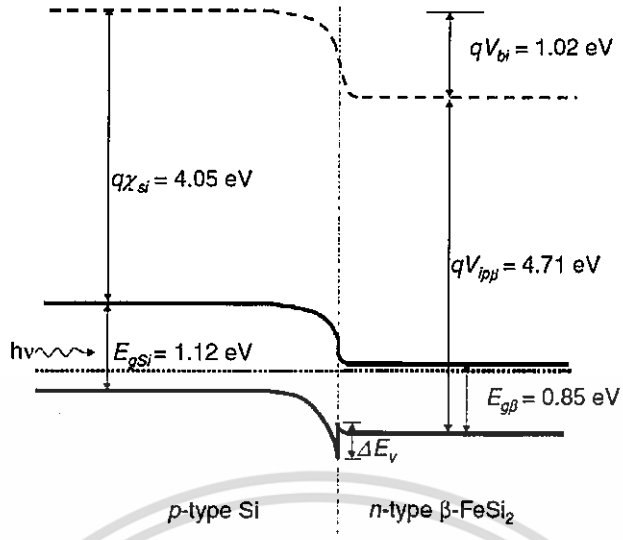

Figure 2.10 Energy band diagram of n-type β-$FeSi_2$/p-type Si heterojunction [41].

In Fig. 2.10, the spike is clearly observed in the valence band, resulting in negative yields from transport mechanism of the carriers. Based on the complex transport mechanism of heterojunction, there is also lattice mismatch problem in between two different semiconductors. This effects to the occurrence of interface states in junction, acting as recombination centers, and enhancing the tunneling current [41]. These actions were a big problem specifically photodiode and photovoltaic devices. However, the benefits of heterojunction structure overcome these problems due to flexible band gap arrangement. For example, capability allows us to choose a high band gap optically transparent window layer, which is utilized in creating solar cell devices. This could help reducing the recombination at the front electrode. Besides, this enhances the short wavelength spectral response and increase photo-generated current.

2.5 Thermionic emission (TE) theory [40, 43-44]

Current flow mechanism across junction of rectifying devices such as conventional diode can be described by TE theory as followed [40]

$$J = J_0\left[\exp\left(\frac{qV}{nkT}\right)-1\right], \tag{2.4}$$

where V, J, T, k, q, n and J_0 are the applied voltage across the heterojunction, the current density, the temperature, Boltzmann's constant, the electron charge, the

heterojunction ideality factor and the saturation current density, respectively. When the J_0 is computed, the ϕ_b value can be computed by the following equation:

$$J_0 = A^* T^2 \exp\left(\frac{-q\phi_b}{kT}\right). \quad (2.5)$$

Based on Eq. (2.4) for the V higher than $3kT/q$, the n can be computed from the slope of the linear part of lnJ-V as follows:

$$n = \frac{q}{kT}\frac{dV}{d(\ln J)} = \frac{q}{kT}\frac{1}{slope}. \quad (2.6)$$

An estimation of the n value following Eq. (2.6) can indicate the characteristics of the carrier conduction mechanisms in a junction. However, the estimated value of n also depends on the chosen range of bias voltage. Therefore, the calculation of n as the functions of temperature should determine the bias range, in order to fit the slope, to be the same range for each temperature range.

2.6 Cheung's method [45]

For the current thesis, the R_s was computed by utilizing the methods developed by several researchers group. The author would like to introduce Cheung method to estimate the R_s. According to Cheung's proposal, the forward I-V characteristics of a schottky diode obeying the thermionic emission model are given by Eq. 2.4. The effect of the R_s is usually modeled with a series combination of a diode and a resistor with resistance through which the current flows. The voltage V_d across the diode can then be expressed in terms of the total voltage drop V across the series combination of the diode and the resistor. Therefore, $V = V_d - IR$, and for $V_d > 3kT/q$, Eq. 2.4 becomes $J = J_0[exp(q(V - IR)/nkT) - 1]$. This equation was differentiated and rearranged as expressed below [45]:

$$\frac{dV}{d(\ln J)} = AR_s J + \frac{nkT}{q}, \quad (2.7)$$

and,

$$H(J) = AR_s J + n\phi_b = V - \frac{nkT}{q}\ln\left(\frac{J}{A^* T^2}\right), \quad (2.8)$$

where R_s, ϕ_b, A^* and A are series resistance, barrier height, Richardson's constant of semiconductor (for $FeSi_2$, A^* = 58.8) and area of junctions, respectively.

2.7 Norde's method [46-48]

On the basis of ideal Schottky-barrier diode equation, for the range of bias voltage $kT/q << V << IR$, difficulties will arise, however, if the base material presents a series resistance to the diode because if R_s is large, this bias voltage range will be too small to give a reliable value of I_0. Besides, on conventional equation, it forces us to choose the range of bias voltage at the small value of V. This results in that recombination current in the diode maybe a significant part of the total current, making the I_0 value still more unreliable. The problem with a series resistance in many cases be avoided by using a relationship developed by Norde as shown below [46-48]:

$$F(V) = \frac{V}{\gamma} - \frac{kT}{q}\ln\left(\frac{J}{A^{*}T^{2}}\right), \tag{2.9}$$

where V, is the applied bias voltage, J is the voltage-dependent forward current density, T is the temperature, and γ is the first integer more than the n value.

Both ϕ_b and R_s values could be computed by estimation of the minimum point of $F(V)$-V as the following equation:

$$\phi_b = F(V_0) + \frac{V_0}{\gamma} - \frac{kT}{q}, \tag{2.10}$$

where $F(V_0)$ is the minimum of $F(V)$, and V_0 is the corresponding voltage, and

$$R_s = (\gamma - n)\frac{kT}{qJ_{\min}A}, \tag{2.11}$$

where A is the area of the heterojunctions and J_{min} is the corresponding current density.

2.8 Junction parameters [39-41, 49-50, 52]

2.8.1 Dark current

In electronic engineering, dark current is the small current that flows through devices such as photodiode when no photons enter the device. It is referred to as reverse bias leakage current in non-optical devices and is present in all diodes. Physically, the dark current components are (i) the recombination current in the neutral regions, (ii) the recombination current in the space charge region and (iii) the recombination current at the interface states between the two materials of heterojunction.

2.8.2 Ideality factor (n)

n is a parameter that indicates the possible carrier transportation mechanism across a junction. The meaning for each n values can be expressed as follows:

A diffusion process exists in the junction in the case of n value equals to one (n = 1). If n is greater than one and lower than or equal to two ($1 < n \leq 2$), a generation-recombination (*G-R*) process exists in the junction. The existence of defects in semiconducting layer possibly generates deep energy levels in the bandgap, which could behave as recombination centers. For this reason, the weak response of NIR light for application in photodiode is likely due to the recombination of photocarriers at the heterojunction interface. If n is greater than two ($n > 2$), a tunneling process is dominant. This is because of the existence of interface states at the heterojunction interface.

2.8.3 Barrier height (ϕ_b)

the ϕ_b is a potential energy barrier for charges formed at a junction. The barriers have rectifying characteristics, suitable for use as a diode. In the case of MS junctions, the ϕ_b at steady state depends on the combination of metal and semiconductor.

2.8.4 Series resistance (R_s)

Ordinarily, the R_s is the vital parameters that affects to the electrical characteristics of junctions. this should be low as possible. In general, it can arise from the different sources, for instance, the contact made by the probe wire to the electrodes, the back contact, a dirt film or particulate matter between the back contact and pedestal, the resistance of the quasi-neutral bulk semiconductor and an extremely nonuniform doping distribution in doped material.

2.8.5 Interface state density (N_{ss})

Based on MS structure, the interface states are the order of atomic dimensions and located between the metal and the semiconductor. The interface states create strong quantum dipoles between the metal and the semiconductor. These quantum dipoles create very large electric field at the junction and can alter the significant amount of potential within the range of atomic length. For the heterojunction devices, interface states in junction acts as recombination centers, and enhance the tunneling current [41]. Therefore, this parameter should be small as possible. Figure 2.13 demonstrates the existence of interface state density in heterojunction interface.

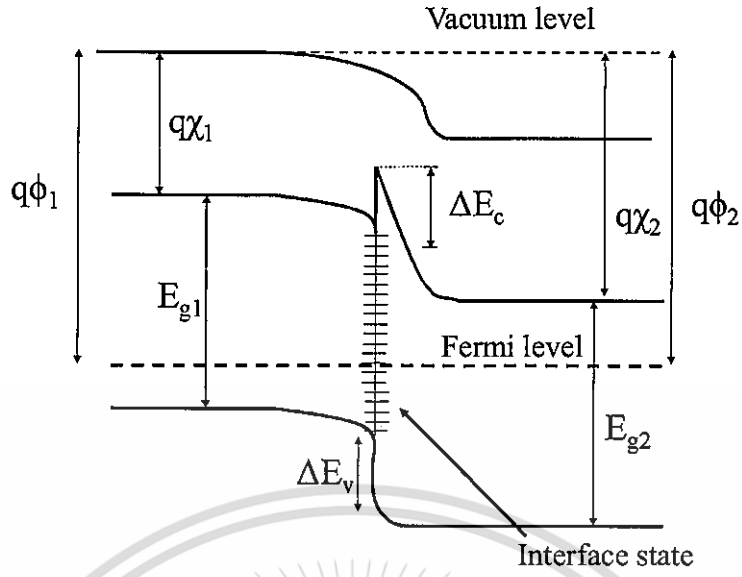

Figure 2.11 The existence of interface state in the heterojunction interface for heterojunction devices.

Chapter 3
Experimental Details

3.1 Chapter overview

The author divided the experimental details into three parts. Firstly, the author will describe the creation of n-type ß-$FeSi_2$/p-type Si heterojunctions by utilizing RFMS including the process of structural and electrical measurements. After that, the creation of n-type NC-$FeSi_2$/i-UNCD/a-C/p-type Si heterojunctions formed by utilizing PLD will be discussed, followed by the explanation of the measurement for their electrical properties. Finally, the details of means to estimate heterojunction parameters will be provided, respectively.

3.2 n-Type ß-$FeSi_2$/p-type Si heterojunctions created by utilizing RFMS

3.2.1 Formation of ß-$FeSi_2$ layer on Si wafer

In this research, ß-$FeSi_2$ layer was formed on Si(111) wafer by utilizing an $FeSi_2$ alloy target. Before the formation of ß-$FeSi_2$ layer, an oxide layer on Si wafers were eliminated by immersion of the Si wafers in diluted hydrofluoric acid (HF) solution. Then, they were cleaned in deionized water. After cleaning, they were set in RFMS system as shown in Fig 3.1.

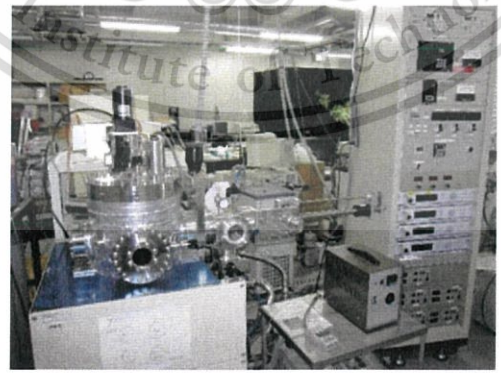

Figure 3.1 RF magnetron sputtering system in Yoshike's laboratory at Kyushu university.

In the formation process, the pressure inside the RFMS chamber was evacuated to 10^{-4} Pa. At a substrate temperature of 560°, ß-$FeSi_2$ layer with a thickness of 300 nm was formed on the p-type Si(111) wafer for 10 hours. The sputtering pressure was 2.66

$\times 10^{-1}$ Pa under Ar atmosphere. RF power tuned by RF auto matching system was 20 W. After the formation of the β-$FeSi_2$ layer on the Si wafer. It was transferred to another RFMS system to form the electrodes. Pd was formed on the front Si wafer in a finger-shaped pattern. Al was coated on the entire back of the β-$FeSi_2$ layer. The author summarized the formation conditions in Table. 3.1.

Table 3.1 The condition to form the β-$FeSi_2$ layer on Si wafer.

Formation process	RFMS
Sputtering target	$FeSi_2$ (Purity: 4N)
Substrate temperature	560 °C
Base pressure	1×10^{-4} Pa
Sputtering pressure	2.66×10^{-1} Pa
Flow rate of Ar gas	10 sccm
RF power	20 W
Formation time	10 hours
Film thickness	300 nm

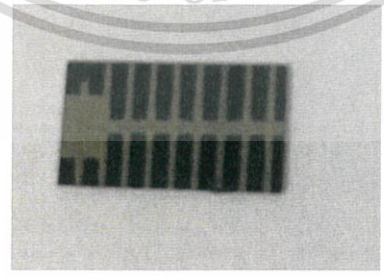

Figure 3.2 An image of n-type β-$FeSi_2$/p-type Si heterojunctions formed by utilizing RFMS at a substrate temperature of 560°.

3.2.2 Structural and electrical measurements

The crystallinity for the formed β-$FeSi_2$ layer was studied by utilizing X-ray diffraction (XRD; Rigaku RINT-2000/PC) as shown in Fig 3.3. The surface morphology was investigated by Scanning Electron Microscope (SEM: Hitachi S-4700 Scanning Electron Microscope) as shown in Fig. 3.4 and Atomic Force Microscope (AFM: ASYLUM RESEARCH Atomic Force Microscopes) as illustrated in Fig. 3.5. The measurement of dark *J–V* curve for the formed junction was operated at low temperatures range of 300-20 K. Keithley 2400 was employed as a source meter as shown in Fig 3.6.

Figure 3.3. X-ray diffraction system (XRD; Rigaku RINT-2000/PC).

Figure 3.4 Scanning Electron Microscope (SEM: Hitachi S-4700 Scanning Electron Microscope).

Figure 3.5 Atomic Force Microscope (AFM: ASYLUM RESEARCH Atomic Force Microscopes)

Figure 3.6 A Source meter (Keithley 2400).

The Thermionic emission (TE) theory, Cheung's and Norde's methods were utilized for computation of junction parameters including the values of n, ϕ_b, J_0 and R_s. By TE theory, the n value can be computed from the slope of the linear part obtained from the plot of ln$J$ versus V. The ϕ_b value can be computed from the J_0 value computed from the straight line intercept of the ln$J$-V at 0 V. In addition, the E_a value can be computed from the slope of the Arrhenius plot of lnJ_0 versus 1000/T. To compute the R_s value by Cheung's method, the relationships of $dV/d(lnJ)$-J and $H(J)$-J were plotted. The value of R_s was computed from the slope of these plots. In addition, the n and ϕ_b values can be computed from the straight line intercept of the $dV/d(lnJ)$-J and the $H(J)$-J, respectively. For confirmation of the agreement and precision of the values of ϕ_b and R_s, Norde's method was utilized. By utilizing Norde's method, the relationship between $F(V)$ and V was plotted to compute the ϕ_b as well as R_s from the minimum point of $F(V)$-V plot.

3.3 n-Type NC-$FeSi_2$/i-UNCD/a-C/p-type Si heterojunctions formed by PLD and CAPD

3.3.1 Creation of i-UNCD/a-C and NC-$FeSi_2$ layers

In the first step, a Si(111) wafer was cleaned in acetone, methanol, and distilled water in sequence. Subsequently, the Si was dipped in a diluted hydrofluoric (HF) acid.

The Si wafer was blown with N_2 gas after rinsing in deionized water. After that, it was set on the substrate holder inside a CAPD chamber that evacuates to a base pressure of 10^{-4} Pa as displayed in Fig. 3.7. A graphite target was utilized as the target of a coaxial arc plasma gun. At room temperature, an i-UNCD/a-C layer with a thickness of 40 nm was grown on a Si(111) wafer. The voltage and capacitance of the capacitor equipped with the arc plasma gun were 100 V and 720 μF, respectively. The repetition rate of pulsed discharge was 5 Hz. After formation of i-UNCD/a-C layer, it was set in a PLD chamber as shown in Fig. 3.8. The inside of the PLD chamber was evacuated to 10^{-6} Torr. A $FeSi_2$ target was used as a target for NC-$FeSi_2$ formation. NC-$FeSi_2$ layer with a thickness of 100 nm was grown on the i-UNCD/a-C layer at room temperature. An ArF excimer laser with a wavelength of 193 nm was employed as the laser source. The Si wafer coated with i-UNCD/a-C layer was placed parallel to the $FeSi_2$ target at a distance of 50 mm. The power and repetition rates of laser pulses were 10 J/cm^2 and 10 Hz, respectively. After that, RFMS apparatus was employed to create metallic electrodes. Al was coated on the NC-$FeSi_2$ layer side. Pd was coated on the Si wafer side. Figure 3.9 illustrates a schematic and image of the n-type NC-$FeSi_2$/i-UNCD/a-C/p-type Si heterojunctions formed by utilizing CAPD and PLD. To understand the deposition process, the author summarized the variable process as shown in table 3.2 and 3.3.

Table 3.2 The formation condition of i-UNCD/a-C layer on Si wafer.

Process	CAPD
Target	graphite
Voltage	100 V
Capacitance of capacitor	720 μF
Substrate	Cz - Si(111) 10-20 Ωcm^{-2}
Substrate temperature	Room temperature
Target to substrate distance	15 mm
Base pressure	10^{-4} Pa
Film thickness	40 nm

Table 3.3 The formation condition of NC-$FeSi_2$ layer on i-UNCD/a-C layer.

Process	PLD
Target	$FeSi_2$
Laser source	ArF excimer laser
Substrate	i-UNCD/a-C layer coated on Si wafer
Substrate temperature	Room temperature
Target to substrate distance	50 mm
Base pressure	10^{-6} Torr
H_2 flow rate	10 sccm
The fluence and repetition rate of the laser pulses	100 mJ and 10 Hz
Film thickness	100 nm

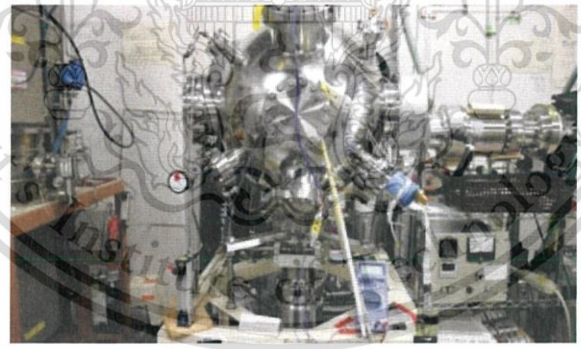

Figure 3.7 CAPD apparatus.

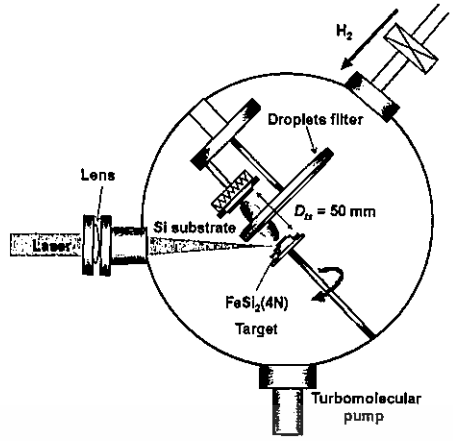

Figure 3.8 Schematic of PLD system.

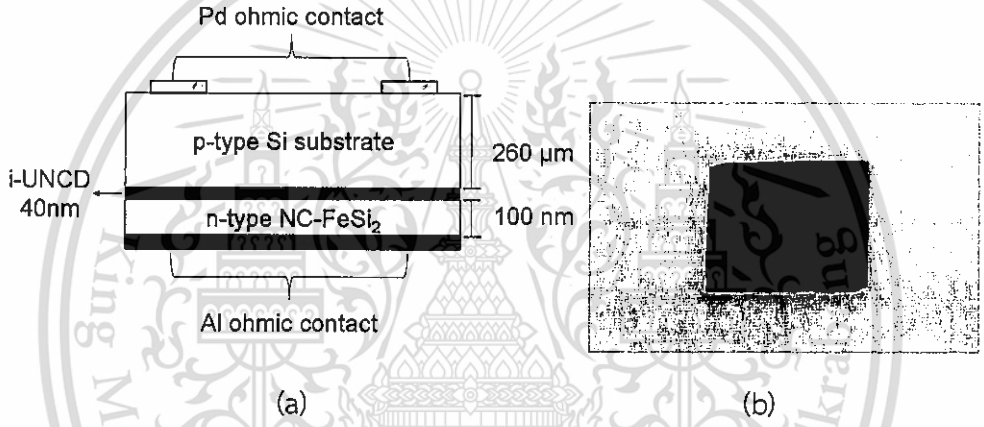

Figure 3.9 (a) Schematic and (b) image of n-type NC-$FeSi_2$/i-UNCD/a-C/p-type Si heterojunctions formed by utilizing CAPD and PLD.

3.3.2 Electrical measurements

Utilizing a source meter (Keithley 2400), the *J-V* curves of the formed heterojunctions were measured in the temperature range from 300 K to 80 K in the dark. The procedures of *I-V* measurement at low temperature have been explained in the topic of 3.4. The heterojunction parameters were computed by TE theory as well as Chueng's and Norde's methods. The explanation of the junction parameter by these theory and methods are the same in the session of n-type ß-$FeSi_2$/p-type Si heterojunctions formed by utilizing RFMS.

3.4 Procedure of *I-V* measurement at low temperature

1) Turn on a water cooling machine until temperature to be 5 °C. The image of water cooling machine was shown in Fig. 3.9.

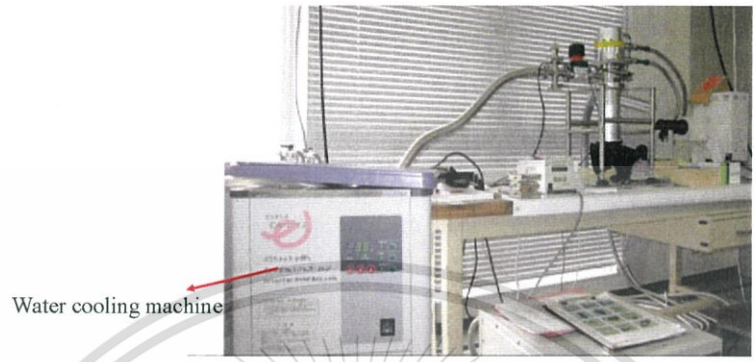

Figure 3.9 Water cooling machine.

2) During the decreasing of water temperature, the formed junction was mounted in a sample holder of cryostat. At the sample holder, there are two gold wires to use in contacting the front and back electrodes of junction in order to apply the bias voltage to the junction together with measure the current at the same time. Both gold wires were connected with a source meter outside the cryostat. The cryostat chamber and the sample holder were shown in Fig. 3.10.

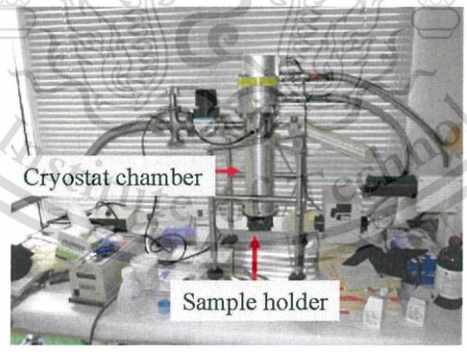

Figure 3.10 Images of cryostat and sample holder.

3) In order to contact the gold wires with the front and back electrodes of the device, the gold wires were mounted in the front and back electrodes by silver paste solder. Two gold wires at sample holder were shown in Fig 3.11.

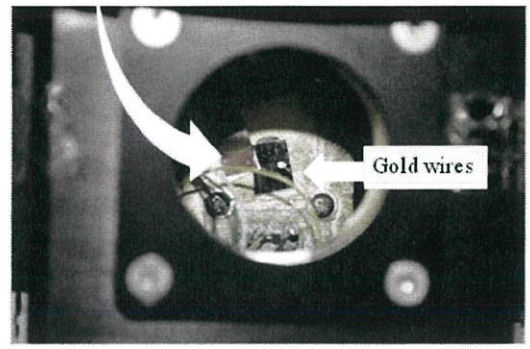

Figure 3.11 Gold wires at sampler holder of cryostat chamber.

4) After silver paste solder dried, the cryostat was evacuated by rotary pump.

5) During the decreasing of pressure inside the chamber, the temperature controller of cryostat machine was set a value of temperature during the *I-V* measurement. Figure 3.12 shows the temperature controller of cryostat machine.

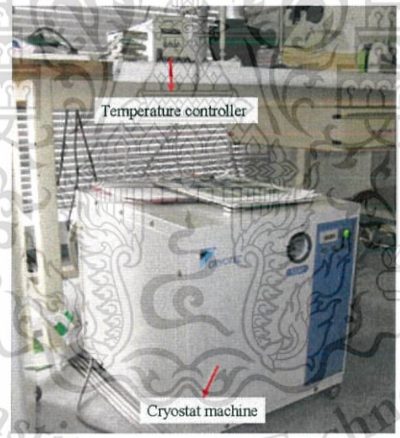

Figure 3.12 A temperature controller of cryostat machine.

6) When the chamber was vacuum and the temperature controller was set, we turned on cryostat machine by pressing the green-light button as shown in Fig 3.12, in order to decrease a temperature inside cryostat.

7) During the decreasing of the temperature inside cryostat until the set value, a source meter was programed. After that, we set the *I-V* measurement variables such as a range of applied bias voltage and step of *I-V* measurement by connecting with a computer. Figures 3.13 shows (a) the source meter, which was connected with the computer, and (b) program to set the variables of *I-V* measurement.

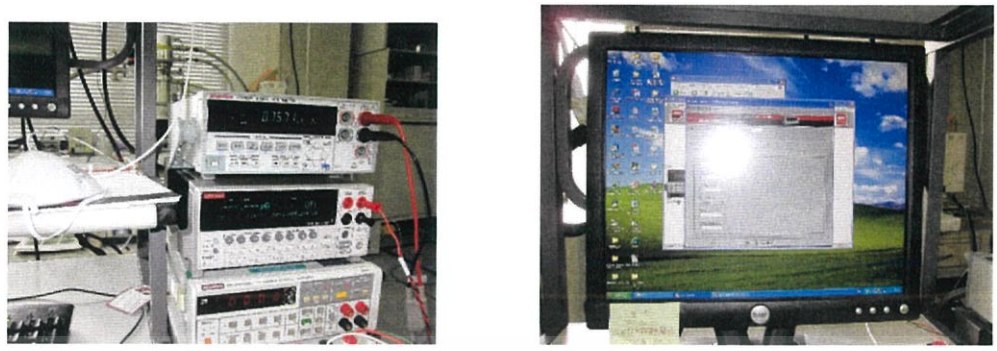

(a) (b)

Figure 3.13 (a) The source meter connected with a computer, and (b) program to set the variables of *I-V* measurement.

8) We measure the *I-V* curve, when the temperature inside the cryostat chamber is equal to that set by step of 6. The data of *I-V* measurement will be saved to be .text files.

3.5 Method for estimation of junction parameters by utilizing TE theory

1) From data of *I-V* measurement, it was plotted via Origin Pro 8.5, which was determined the x-axis as a bias voltage and y-axis as a semi-logarithm current density.

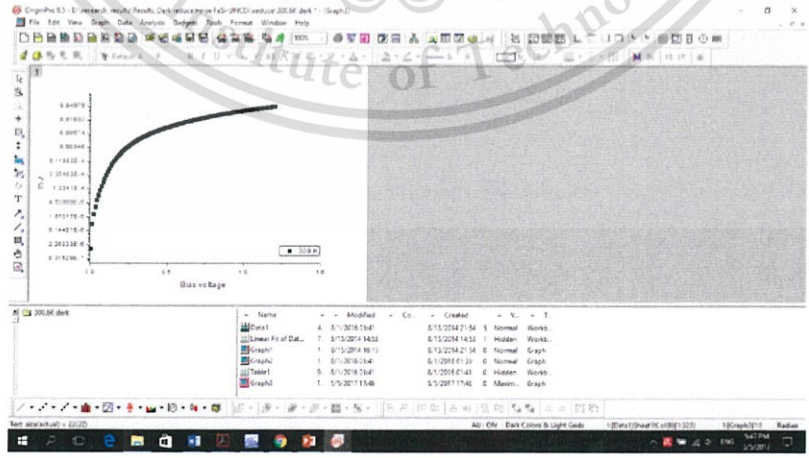

Figure 3.14 *J-V* curve plotted by Origin Pro 8.5.

2) From this plot, we will see the linear variation between current and bias voltage at bias voltage lower than 0.2 V. According to this variation, it can be found the slope of straight line by a fitting function of the program as shown in Fig.3.15.

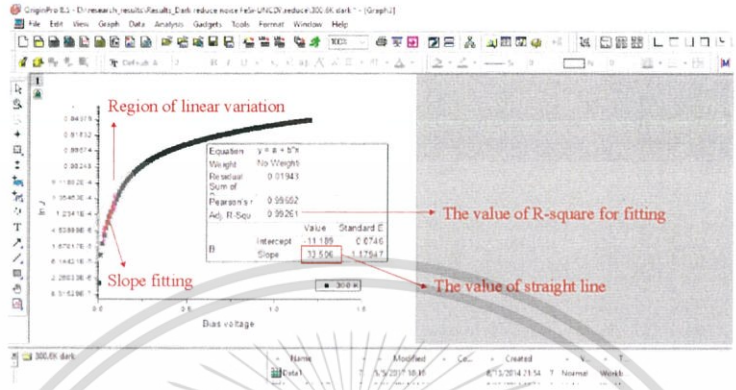

Figure 3.15 Fitting to find the slope of *J-V* curve.

3) After that, we put the value of slope into Eq. 2.6. to calculate the value of *n* parameter.

4) From Fig. 3.15, if we draw extra linear line from slope line (blue line) to intercept in y-axis, we will obtain the value of J_0 as shown in Fig. 3.16. After that, we use the value pointer function in Origin Pro 8.5 to read the value of J_0 at y-axis intersection point.

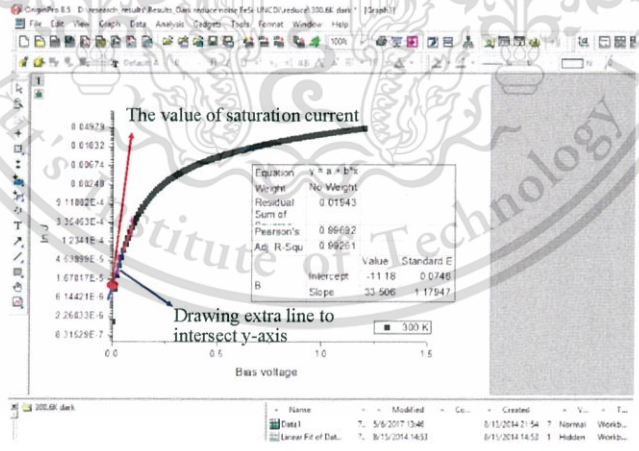

Figure 3.16 Drawing of extra linear line to find the value of J_0 from *J-V* curve.

5) According to step 4), we will obtain the value of J_0. The ϕ_b can be calculated by substitution of the value of J_0 into Eq. 2.5.

3.6 Procedure for estimation of junction parameters by Cheung method

1) When we obtained *J-V* data from the measurement, we used Eq. (2.7) and (2.8) to compute the values of d*V*/dln*J* and H(*J*) functions, respectively.
2) When we knew the values of both functions, we plotted the relation of the both values versus *J* value measured from *J-V* measurement as shown in Fig. 3.16.

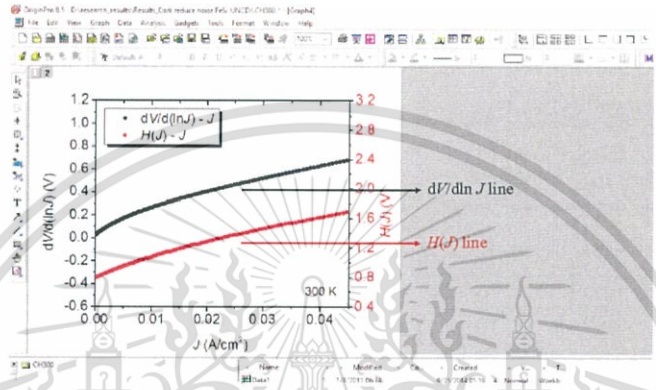

Figure 3.17 The plot of d*V*/dln*J* and *H(J)* versus *J* value.

3) As seen in Fig. 3.17, the plots were straight lines. Here, d*V*/dln*J* was black line and *H(J)* was red line. Now, we can find the slope of both lines by using a function of linear fitting in Origin Pro 8.5.
4) We will obtain the values of slopes as seen in Fig. 3.18.

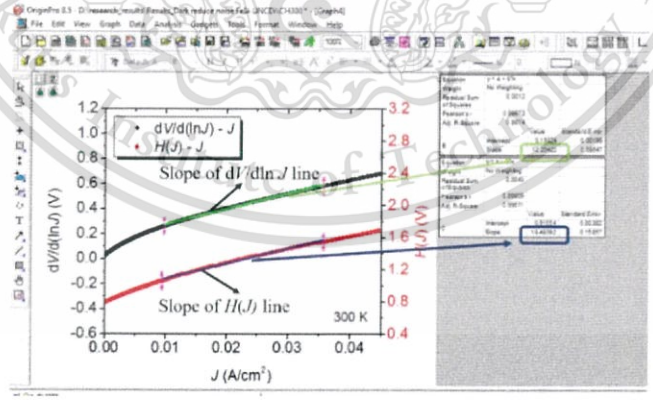

Figure 3.18 Estimation of slopes of d*V*/dln*J* and *H(J)* lines.

5) Either d*V*/dln*J* or *H(J)* slopes can give the value of R_s through Eq. 2.7 and 2.8, respectively.
6) Furthermore, for d*V*/dln*J* line, if we draw extra straight line to intersect y-axis, the intersection point can be calculated via Eq. 2.7 to find the value

of *n*. At the same way, for *H(J)* line, the value of ϕ_b is also calculated via Eq. 2.8 (note that *n* value in Eq. 2.8 is given by Eq. 2.7).

3.7 Procedure for estimation junction parameters by Norde method

1.) At first, we calculated the value of *F(V)* by using Eq. 2.9 from the measured *J-V* data.
2.) When we knew the value of *F(V)*, we plotted this value versus *V* value as seen in Fig. 3.19.
3.) As shown in Fig. 3.19, we see the line as parabola function, and will see a minimum point of this curve.
4.) We used a Data reader tool in Origin Pro 8.5 to read the minimum point. This value was called "$F(V_0)$" and V_0 at corresponding bias voltage.

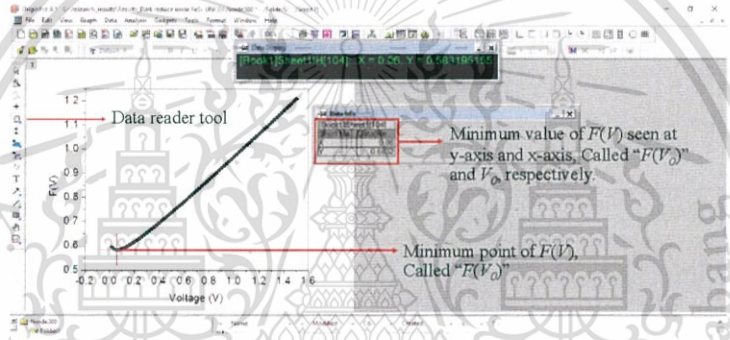

Figure 3.19 The plot of *F(V)* versus *V* value.

5.) With $F(V_0)$ and V_0 values, we can compute the value of ϕ_b by using Eq. 2.10.
6.) With V_0 value, it makes us find the corresponding value of *J* in measured *J-V* data in Excel file as shown in Fig. 3.20. This current density is called "J_{min}".
7.) When we knew the value of J_{min}, the value of R_s can be computed by using Eq. 2.11.

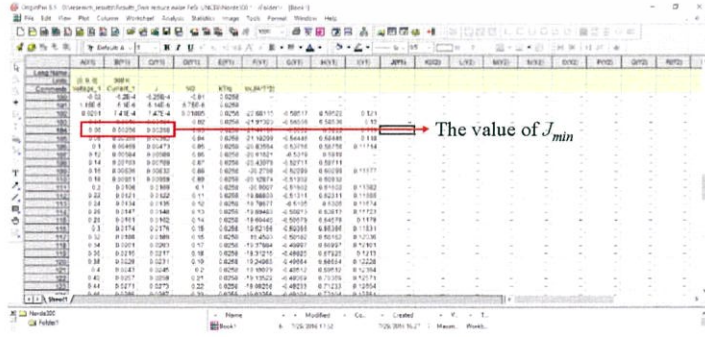

Figure 3.20 Estimation of J_{min} via the value of V_0.

Chapter 4
Results and discussion

4.1 Chapter overview

In this chapter, the author would divide the details of results to two parts. Firstly, the result of computation of junction parameters at low temperatures in the heterojunctions comprising n-type β-fesi$_2$ layer and p-type Si(111) wafer formed by RFMS will be explained. After that, the characterization of junction parameters in n-type NC-FeSi$_2$/i-UNCD/a-C/p-type Si heterojunctions will be discussed in detail.

4.2 Computation of junction parameters at low temperatures in heterojunctions comprising n-type β-FeSi$_2$ layer and p-type Si(111) wafer

4.2.1 Structural features of n-type β-FeSi$_2$ layer on p-type Si(111) wafer

Figure 4.1(a) illustrates the XRD diffraction pattern of β-FeSi$_2$ layer formed by RFMS on Si(111) wafer at a substrate temperature of 560 °C. From the pattern, we can observe a weak 404/440 diffraction peak as well as strong 202/220 diffraction peak. These observed peaks are typical peaks for epitaxial growth of β-FeSi$_2$ on Si(111). Fig. 4.1(b) demonstrates a pole figure pattern for the β-440/404 peak. The formed β-FeSi$_2$ layer demonstrated the appearance of three epitaxial variants that are rotated by an angle of 120° with respect to each other.

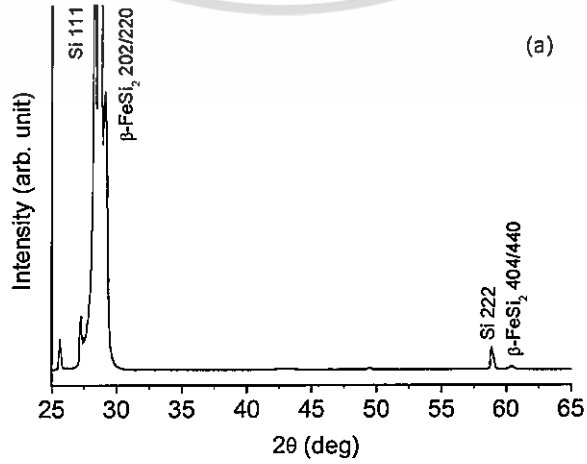

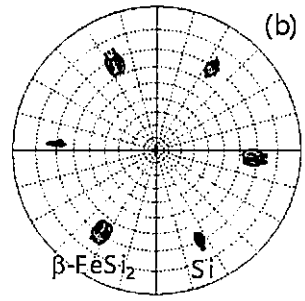

Figure 4.1 (a) XRD pattern of β-$FeSi_2$ layer formed on Si(111) wafer and (b) a pole figure pattern of the β-440/404 diffraction peak.

Figure 4.2 (a) demonstrates the SEM micrograph in plane view of the surface of β-$FeSi_2$ layer formed by RFMS on Si(111) wafer. The formed β-$FeSi_2$ layer is composed of a large amount of crystallites with the small size. Figure 2 (b) illustrates a cross-sectional SEM micrograph for the β-$FeSi_2$ layer. This micrograph exhibited a sharp interface between Si layer and β-$FeSi_2$ layer. Furthermore, the β-$FeSi_2$ layer was uniform.

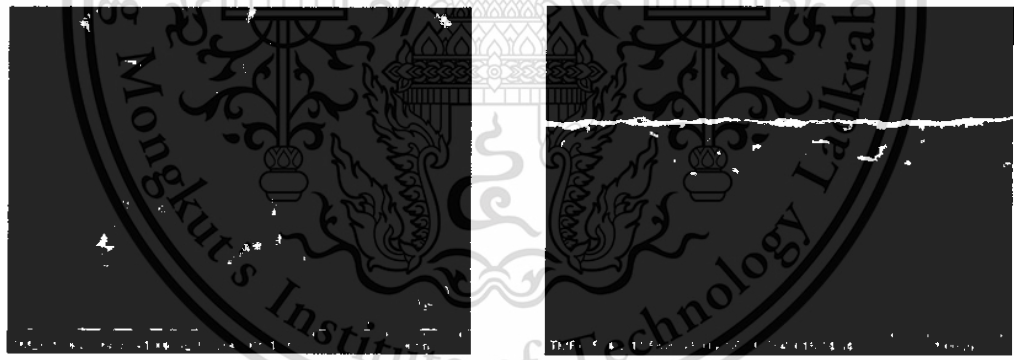

Figure 4.2 (a) SEM micrograph of the surface for β-$FeSi_2$ layer formed by RFMS on Si(111) wafer and (b) cross-sectional SEM micrograph of β-$FeSi_2$ layer on Si(111) wafer.

Figure 4.3 displays the AFM image in the three-dimension of β-$FeSi_2$ layer formed on Si(111) wafer. From the image, a root-mean-square (RMS) roughness of the β-$FeSi_2$ is 17.56 nm. A large RMS value should be because the β-$FeSi_2$ wafer was placed in the plasma during formation of β-$FeSi_2$ layer by RFMS.

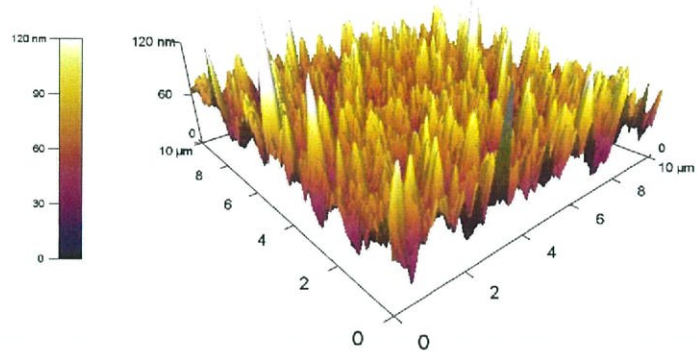

Figure 4.3 AFM image of the surface for ß-$FeSi_2$ layer formed by RFMS on Si(111) wafer.

4.2.2 Junction parameters at low temperatures of heterojunctions comprising n-type ß-$FeSi_2$ layer and p-type Si(111) wafer

The dark *J-V* curves of the n-type ß-$FeSi_2$/p-type Si heterojunctions formed by RFMS as a function of temperature range of 300-20 K are displayed in Fig. 4.4. From particular consideration at room temperature, the heterojunctions exhibited a clear rectifying action similar to conventional pn abrupt junctions, which is due to the successful formation of a junction between ß-$FeSi_2$ layer and Si wafer. Furthermore, this rectifying action evidently improved at low temperatures. However, the ß-$FeSi_2$/Si heterojunctions had a large leakage current at room temperature. This is likely because of the partially-diffused Fe atoms in the depletion region of the Si side acting as leakage centers for the carriers [29]. This leakage current diminished at low temperatures.

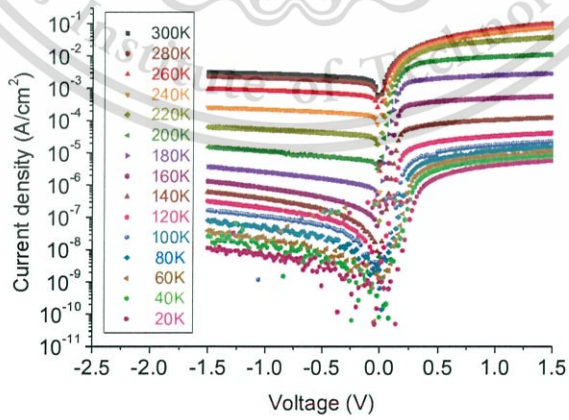

Figure 4.4 Semi-logarithmic plot of the dark *J–V* curves of the heterojunctions under forward and reverse bias conditions at temperatures from 300 down to 20 K.

From consideration of the region of V value ≤ 0.2 V, the forward J value exhibited a linear change with the V value. This can be described by means of the TE theory as the following relationship [40]:

$$J = J_0\left[\exp\left(\frac{qV}{nkT}\right)-1\right]$$

where V is the applied bias voltage across the junction, J is the current density, T is the absolute temperature, k is Boltzmann's constant, q is the electron charge, and J_0 is the saturation current density, which can be computed from the straight line intercept of the y-axis of ln(J)-V at 0 V. After the value for J_0 is computed, the ϕ_b value can be computed by the following equation:

$$J_0 = A^* T^2 \exp\left(\frac{-q\phi_b}{kT}\right)$$

n is the heterojunction ideality factor. For the V value higher than $3kT/q$, we can compute the n value from the slope of the linear part of ln(J)-V as follows equation:

$$n = \frac{q}{kT}\frac{\mathrm{d}V}{\mathrm{d}(\ln J)} = \frac{q}{kT}\frac{1}{\text{slope}}$$

Estimation of the n value following above equation can indicate the carrier transportation mechanism across junctions. If it equals unity, the junction is ideal. Conversely, the junction is flawed if the value of n increases. In the case of the n value being equal to one, the transport mechanism across the junction of the carrier is governed by a thermal diffusion process. If the n value is greater than one and lower than or equal to two, the transport mechanism of the carrier is dominated by a generation-recombination (G-R) process. Besides, the transport mechanism of the carrier is probably governed by a tunneling process if the n value is greater than two [40,52].

Figure 4.5 illustrates a plot of n versus the temperature for the formed heterojunctions. By computation utilizing Eq. (2.6), the n value at 300 K was 1.71. The n values remained nearly constant at a temperature ranging from 300 to 120 K. In this case, the n value was greater than one and lower than two. The transportation mechanism across the junction of the carrier should be governed by a G-R process at the β-$FeSi_2$/Si heterojunction interface. The existing defects in the β-$FeSi_2$ layer might create deep energy levels in the bandgap, which behave as recombination centers. The n value was computed 3.25 at a temperature of 100 K. It increased to 16.83 at 20 K. In this case, the n value was higher than two. Thus, the transportation mechanism across the junction of the carrier should be governed by a tunneling process. This should be due to the existing interface states at the interface of junctions. The

heterojunctions possess a large value for *n*, which is likely owing to the presence of a flawed contact behavior as well as the result of inhomogeneity and tunneling [49]. Mathematically, R-square is a statistical value which suggests that how close the data are to the fitting line. The R-square is always between 0 and 1. If the fitting line has the R-square value close to 1, this indicates that the fitting line slightly deviates from the data. Namely, the R-square can imply the reliability of the fitting line in the experiment. The author summarized the estimated values by TE theory such as *n*, slope, J_0, and range of *V*, which was used to draw the linear line in TE regime, as well as the R-square value into table. 4.1.

In addition, the simulation of *J-V* curves in the TE regime was completed by utilizing MATLAB program in order to check the consistency of the estimated junction parameters. Figure 4.6 shows comparison between *J-V* curves from measurement and from MATLAB fitting at (a) 300 K and (b) 20 K. According to Fig. 4.6 (a) and (b), the *J-V* curves simulated by MATLAB (red line) are very nearly the same tendency with that measured from experiment (black line).

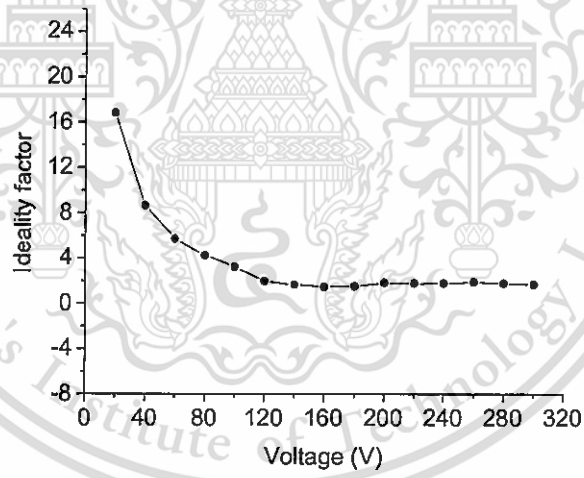

Figure 4.5 Plot of the *n* value versus temperature.

Table 4.1 The values of *n*, slope and J_0 estimated by TE theory method.

T (K)	*n*	Slope	J_0 (A/cm$_2$)	R-Square	Range (V)
20	16.8305	34.4870	9.93E-12	0.99838	0.16-0.30
40	8.6565	33.4840	4.71E-11	0.99225	0.16-0.26
60	5.7234	33.8042	1.55E-10	0.98374	0.08-0.22

80	4.2679	33.9999	4.42E-10	0.99205	0.08-0.24
100	3.2579	35.6314	1.00E-09	0.95984	0.04-014
120	1.9981	48.4149	1.46E-09	0.99779	0.02-0.14
140	1.6713	49.6131	1.08E-08	0.99372	0.06-0.16
160	1.5004	48.3549	1.05E-07	0.99502	0.06-0.14
180	1.5596	41.3001	7.22E-07	0.98277	0.04-0.16
200	1.9973	31.6190	1.24E-06	0.97397	0.06-0.16
220	2.3465	29.5611	4.80E-05	0.96978	0.04-0.14
240	2.1568	26.5775	1.15E-04	0.93753	0.02-0.14
260	1.8952	23.5544	3.37E-04	0.93625	0.02-0.12
280	1.7778	23.3203	5.00E-04	0.93924	0.02-0.10
300	1.7178	22.5252	5.34E-04	0.93854	0.02-0.10

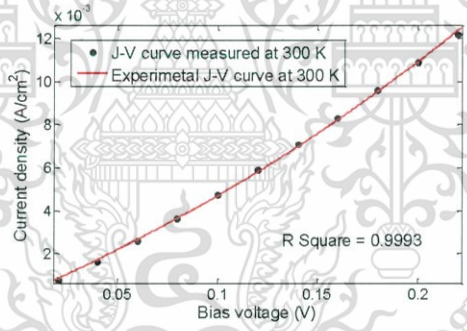

(a)

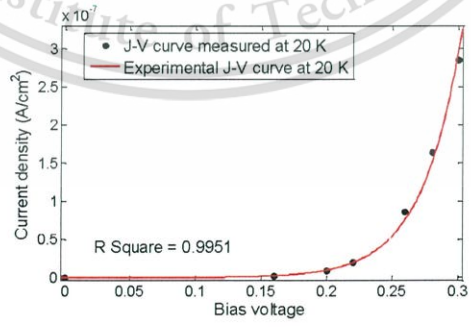

(b)

Figure 4.6 The comparison between *J-V* curves from the measurement (black line) and from MATLAB fitting (red line) at (a) 300 K and (b) 20 K.

When the J_0 values is estimated, the value of E_a can be computed by the following relation [48,50-51]:

$$J_0 \propto \exp\left(\frac{\Delta E_a}{kT}\right).$$

Figure 4.7 illustrates an Arrhenius plot between lnJ_0 and 1000/T. The J_0 values were 5.34 × 10^{-4} A/cm^2 at room temperature and 9.93 × 10^{-12} A/cm^2 at 20 K. The two regions from the plot indicate that there are two values for E_a. The slopes for each region can compute the values of E_a. Between 300 and 140 K, the recombination process is predominant with an E_a value of 0.24 eV. The carrier tunneling process is predominant with an E_a value of 9.18 meV below 140 K. After the computation of the J_0 value, the ϕ_b value is computed utilizing Eq. (2.5).

Figure 4.8 shows the plot of ϕ_b versus temperature. The ϕ_b value was 0.59 eV at 300 K. This value decreased to 0.06 eV at 20 K. From the experimental results, the value of n increased and the value of ϕ_b decreased at low temperatures. This is likely because of barrier height inhomogeneity, this should be attributed to the variation in thickness and composition of the interfacial layer as well as non-uniformity of the interfacial charges [53-54].

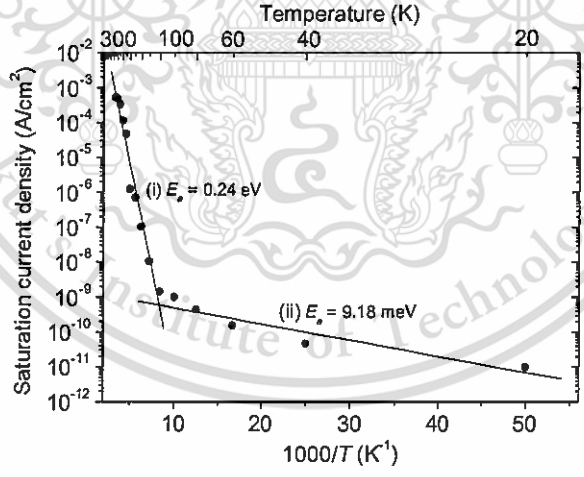

Figure 4.7 Arrhenius plot for log J_0 versus 1000/T.

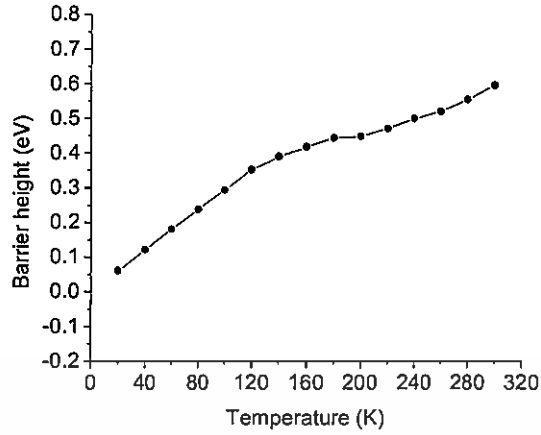

Figure 4.8 A plot of the ϕ_b value versus temperature.

For the current study, the R_s value was computed by utilizing methods proposed by Cheung. The equation based on Cheung's method can be expressed as [45]:

$$\frac{dV}{d(\ln J)} = AR_sJ + \frac{nkT}{q}$$

and

$$H(J) = AR_sJ + n\phi_b = V - \frac{nkT}{q}\ln\left(\frac{J}{A^*T^2}\right)$$

where R_s, ϕ_b, A^* and A are series resistance, barrier height, Richardson's constant of β-$FeSi_2$ and area of heterojunctions, respectively.

According to Eq. (2.7), the d*V*/d(ln*J*)-*J* was plotted (left axis) at (a) 300 K and (b) 20 K as displayed in Fig. 4.9. The *nkT/q* was computed from the intercept of y-axis, while the AR_s was computed from the slope. In addition, we plotted the *H(J)-J* (right axis) to confirm the accuracy of R_s value based on Eq. (2.8). the *H(J)–J* at 300 K and 20 K are shown in Fig. 4.9 (a) and (b). The values for AR_s and $n\phi_b$ were computed from the slope and intercept point of the y-axis, respectively. From the computations, the *n* values were 1.63 at 300 K and 16.13 at 20 K. The ϕ_b values were 0.54 eV at 300 K and 0.05 eV at 20 K. These values are in agreement with those computed from the TE theory. Moreover, the R_s values computed from the d*V*/d(ln*J*)–*J* were 13.05 Ω at 300 K and 0.14 MΩ at 20 K. From the slope of *H(J)–J*, the R_s values were 13.18 Ω at 300 K and 0.14 MΩ at 20 K. The R_s values computed from the d*V*/d(ln*J*)–*J* agreed to those computed from the *H(J)–J*. Additionally, the R_s value increased when the temperature was increased. It is likely because of the increasing of *n* under cooled condition.

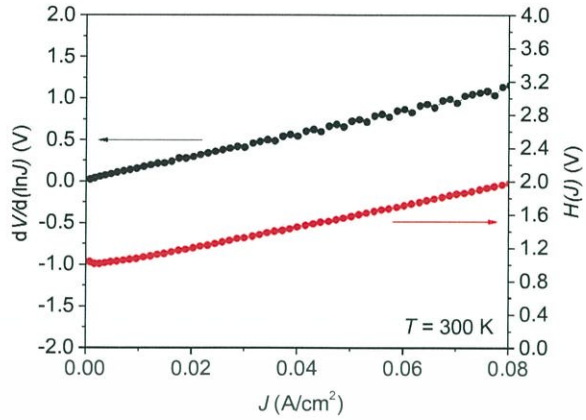

(a)

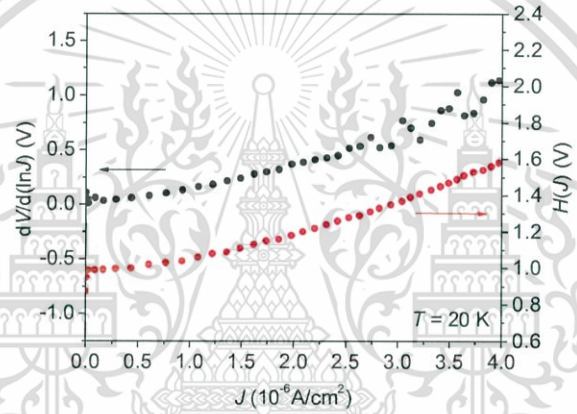

(b)

Figure 4.9 The plot of d*V*/d(ln*J*)–*J* (left-axis) and *H*(*J*)-*J* (right-axis) at temperatures of (a) 300 K and (b) 20 K.

Besides, the current study utilized Norde's method to compute the R_s value. The relationship based on Norde's method is derived as [46-48]:

$$F(V) = \frac{V}{\gamma} - \frac{kT}{q}\ln\left(\frac{J}{A^{*}T^{2}}\right),$$

where V is bias voltage, J is the voltage-dependent forward current density, T is temperature, and γ is the first integer higher than the n value. Both the ϕ_b and R_s values could be computed by estimation of the minimum of $F(V)$-V as follows:

$$\phi_b = F(V_0) + \frac{V_0}{\gamma} - \frac{kT}{q},$$

where $F(V_0)$ is the minimum of $F(V)$, and V_0 is the corresponding voltage, and

$$R_s = (\gamma - n)\frac{kT}{qJ_{\min}A},$$

where A is the area of the heterojunctions and J_{min} is the corresponding current density.

The plots of $F(V)$-V at temperatures of 300 K (red line) and 20 K (black line) are displayed in Fig 4.8. From the plot at 300 K, the values for $F(V_0)$ and V_0 were 0.58 and 0.05 V, respectively. The values for $F(V_0)$ and V_0 at 20 K changed to 0.06 and 0.26 V, respectively. Based on the computation using Eq. (2.10), the ϕ_b values were 0.58 eV at 300 K and 0.07 eV at 20 K. In addition, R_s value computed by Eq. (2.11) was 10 Ω at 300 K and enhanced dramatically to 0.15 MΩ at 20 K. The results from computation using Norde's method were in agreement with those computed by the TE theory and Cheung's method.

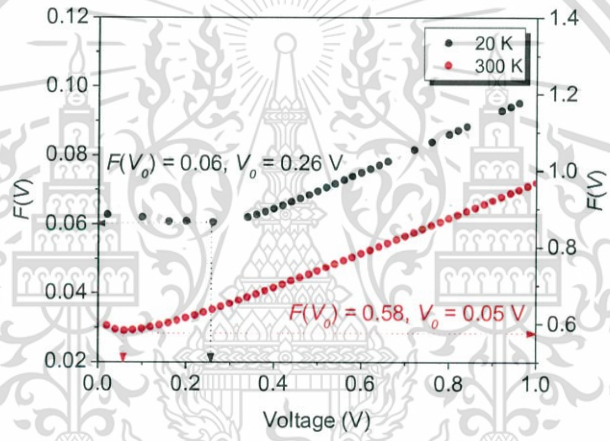

Figure 4.10 Plots of $F(V)$–V at 20 K (left-axis) and at 300 K (right-axis).

At low temperatures, the ratio between the photocurrent to dark current was increased, which was probably due to the reduction of the reverse leakage current at low temperatures [31]. This reduction of leakage current is attributable to the decreased carrier densities in the ß-$FeSi_2$ layer at low temperatures [11,31,39]. Unexpectedly, the photocurrent decreased along with the decrease of the leakage current at low temperatures [31]. Based on the computation of the n value, this value increased to be > 2 at low temperatures. This might imply that a tunneling process contributed to the carrier transportation mechanism [39]. This is likely owing to the existence of interface states at the heterojunction interface [39]. The existent interface states could behave as a trap center of photo-generated carriers [11], which would be the possible cause for the reduction of photocurrent at low temperatures. Additionally, we consider that the carrier tunneling process implies the appearance of spikes in conduction and valence bands owing to a heterojunction band offset as shown in Fig.

4.9. These spikes prevent the flow of photo-generated carriers at the heterojunction interface. The decreased photocurrent at low temperatures might be because the spikes that appear in conduction and valence bands are higher at low temperatures and they could behave as a barrier for the photo-generated carriers flowing at the heterojunction interface. It is expected that the spikes were enlarged at low temperatures owing to the Fermi levels of Si and ß-$FeSi_2$ layers approaching the center of the band gaps at low temperatures. Also, from the computation of the R_s, this parameter increased at low temperatures. This might be attributable to the low mobility of carriers in the ß-$FeSi_2$ layers, which degrades at low temperatures [55].

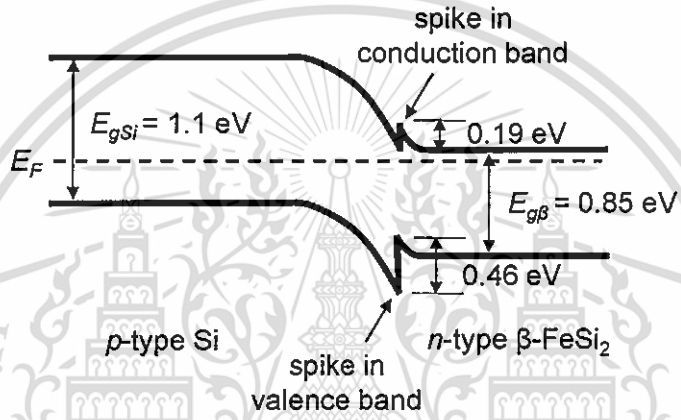

Figure 4.11 Energy band diagram that indicates the spikes in conduction and valence bands for n-type ß-$FeSi_2$/p-type Si heterojunctions.

4.3 Characterization of junction parameters in n-type NC-$FeSi_2$/i-UNCD/a-C/p-type Si heterojunctions

4.3.1 Structural characteristics of NC-$FeSi_2$ layer grown on i-UNCD formed on Si wafer by utilizing PLD

Figure 4.12 exposes the surface morphology of the NC-$FeSi_2$ layer formed on Si(111) wafer. The image displayed that the formed layer plentifully consisted of circlet-crystallites with diameters of 4-6 nm. Moreover, the great smooth surface of the layer in nanoscale with no pinholes was observed as displayed in Fig. 4.12.

Figure 4.12 Plane-view SEM image of the NC-$FeSi_2$ layers grown on Si substrate by utilizing PLD at room temperature.

4.3.2 Electrical characteristics of n-type NC-$FeSi_2$/i-UNCD/a-C/p-type Si junctions

The characterizations of dark *J-V* characteristics for the pin heterojunctions in this report have provided valuable information about junction parameters, such as rectification ratio and the values of n, ϕ_b and R_s. Figure 4.13 displays the dark *J-V* curves in linear scale for the prepared heterojunctions measured at room temperature. The heterojunctions shows rectifying behavior similar to conventional *pn* abrupt junctions with a turn-on voltage of 0.12 V.

Figure 4.14 illustrates the dark *J-V* curves for the prepared heterojunctions, which were measured under forward and reverse bias voltages at low temperatures ranging between 300 K and 80 K. At room temperature, the heterojunctions showed rectifying action along with a large leakage current. At 80 K as compared with that at room temperature. This leakage current was reduced by more than three orders of magnitude. This was likely due to the decreasing of carrier density for NC-$FeSi_2$ layer under cooled conditions.

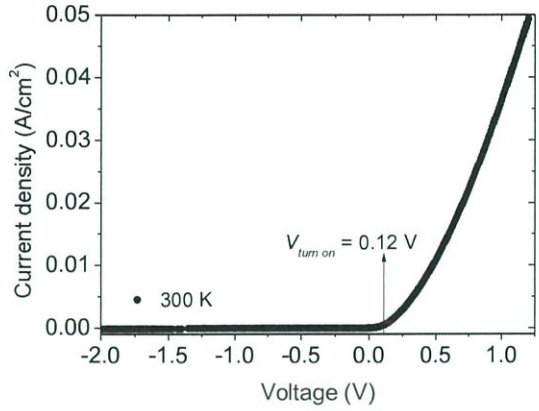

Figure 4.13 Dark *J-V* curves in linear scale for the prepared heterojunctions measured at room temperature.

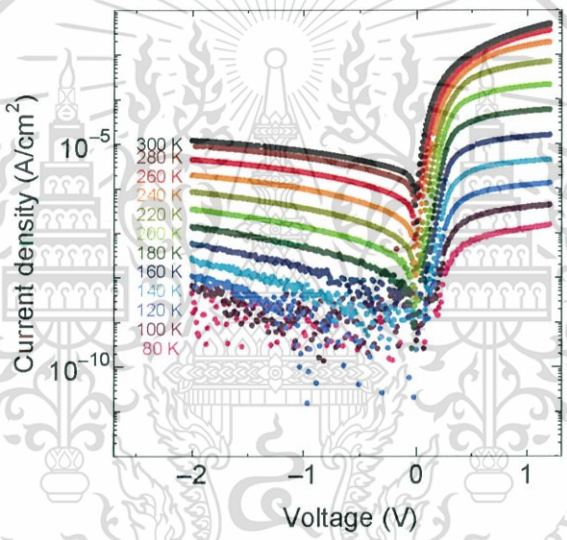

Figure 4.14 *J-V* curves for the heterojunctions measured under forward and reverse bias voltage conditions at low temperatures.

In order to calculate the n, J_0 and R_s for the n-type NC-$FeSi_2$/i-UNCD/a-C/p-type Si heterojunctions, we utilized the relation based on TE theory, Cheung's and Norde's methods as explained in the first part.

Here, we start from the explanation of the result that were estimated by TE theory. The plot between the n value and temperature for the heterojunctions is illustrated in Fig. 4.15. The n value at 300 K was 1.12 and gradually increased to 1.99 at 180 K. The n values in this temperature range were in the case of $1 < n \leq 2$. Thus, the probable transport mechanism of the carrier across the interface of the junctions is a recombination process [40,52]. The existence of defects in NC-$FeSi_2$ layer may generate deep energy levels in the bandgap. These energy levels could behave as

centers of recombination. When the temperature decreased to 160 K, the *n* value was 3.25. It increased to 5.44 at 80 K. In the case of *n* values > 2, the tunneling process should be governed across the interface of the heterojunctions [60]. This can be attributable to the existent interface states at the interface of the junctions. A large *n* value of heterojunctions might be due to the presence of non-ideal contact behavior and the result of the barrier inhomogeneity [54].

The plot between the ϕ_b value versus temperature is shown in Fig. 4.16. The ϕ_b value was 0.69 eV at 300 K and decreased to 0.24 eV at 80 K. From the experimental results, the value of *n* increased and the value of ϕ_b decreased at low temperatures.

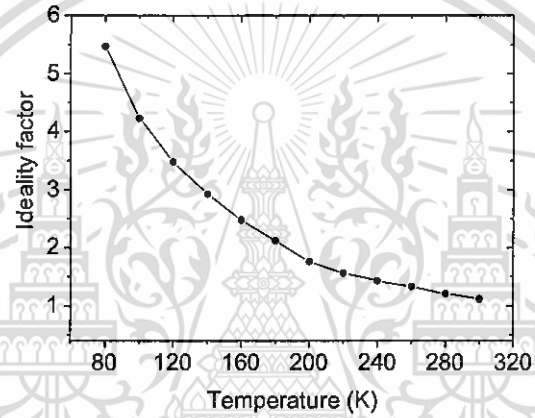

Figure 4.15 Plot between *n* value and temperature for the prepared heterojunctions.

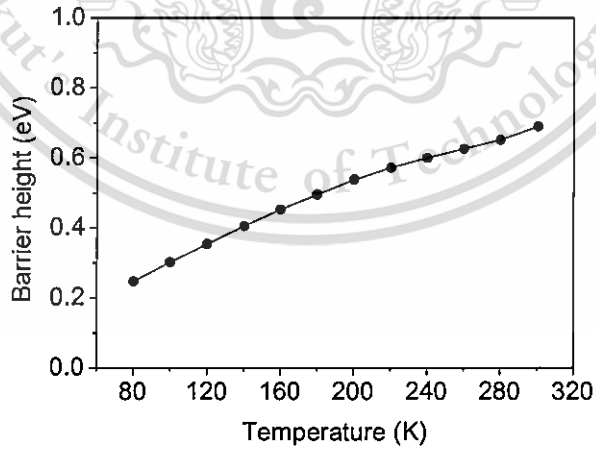

Figure 4.16 The plot between the ϕ_b value and temperature.

Here, we report the estimation of R_s, *n* and ϕ_b for the heterojunctions based on Cheung's method. This method was explained in the previous part. Figure 4.17 presents the *dV/d(lnJ)* (left vertical axis)–*J* in the black line and *H(J)* (right vertical axis)–*J* in the orange line at (a) 300 K and (b) 80 K. According to the *dV/d(lnJ)*–*J*, the *n* values

were 1.12 at 300 K and 5.46 at 80 K. Additionally, the R_s values were 306.46 Ω at 300 K and 4.25 MΩ at 80 K. The ϕ_b and R_s values computed from the *H(J)–J* were 0.71 eV and 300.88 Ω at 300 K, and 0.23 eV and 4.29 MΩ at 80 K. From the results, the R_s value from the plot of *dV/d(lnJ)–J* is approximately equal to that from the *H(J)–J*.

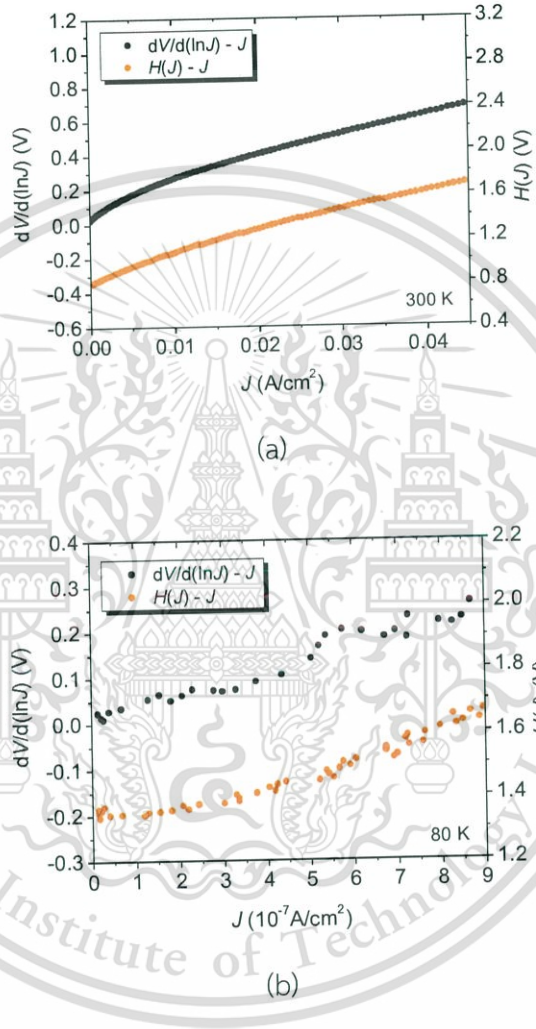

Figure 4.17 The *dV/d(lnJ)* (left vertical axis)–*J* in the black line and H(*J*) (right vertical axis)-*J* in the orange line at temperatures of (a) 300 K, (b) 80 K.

For the final part of estimation, we explained the results that obtained based on Norde's method. Figure 4.18 shows the *F(V)-V* at (a) 300 K and (b) 80 K utilizing Eq. (4.16). From these plots, the ϕ_b and R_s values were calculated following Eq. (2.10) and (2.11), respectively. The obtained ϕ_b values were 0.69 eV at 300 K and 0.27 eV at 80 K. The obtained R_s values were 352.26 Ω at 300 K and 2.52 MΩ at 80 K.

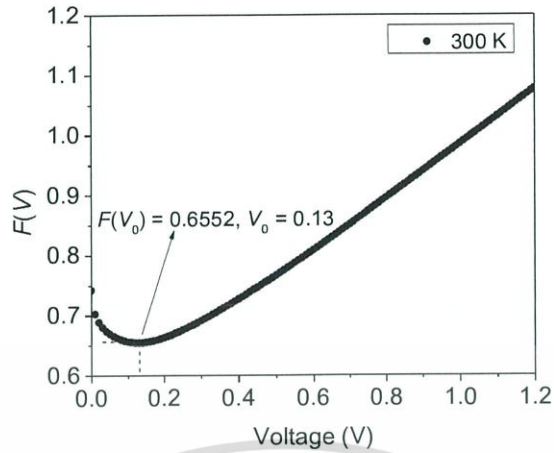

(a)

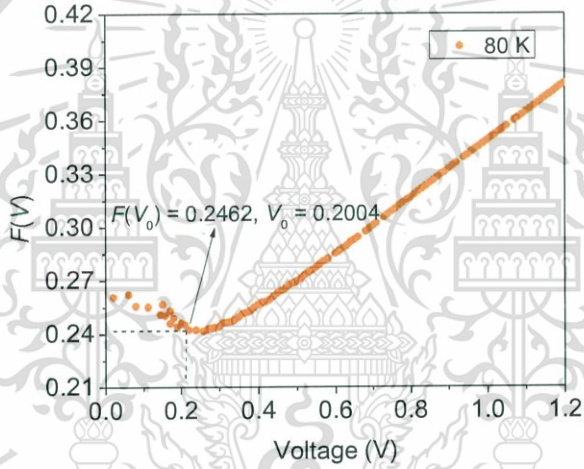

(b)

Figure 4.18 The *F(V)–V* for the heterojunctions at (a) 300 K and (b) 80 K.

Figures 4.19 (a), (b) and (c) show the comparison of heterojunction parameters, including the n, ϕ_b and R_s values computed by TE theory, Chueng's and Norde's methods. From Fig. 4.19 (a), the n value computed by TE theory increases with increasing temperature and agrees very well with the results by Cheung's method. Figure 4.19 (b) illustrates the ϕ_b value computed utilizing the three aforementioned methods. From Fig. 4.14 (b), the ϕ_b values obtained using the three methods showed a similar trend. Specifically, the ϕ_b value from all plots decreases when temperature decreases. These behaviors are probably due to non-uniformity of the interfacial charges at the hetero-interface and inhomogeneity in the barrier of the material [28]. Additionally, the R_s value computed in Fig. 4.14 (c) using Norde's method agrees well with those computed by Cheung's method (Both d*V*/dln*J*-*J* and *H*(*J*)-*J* plots). The

obtained R_s value likely presents in the neutral regions and ohmic contacts. Commonly, the R_s of a junction is an important parameter that affects the electrical characteristics. Thus, it should be kept as low as possible. For the present junction, R_s was found to increase significantly at low temperatures. This can be attributed to low carrier mobility in the NC-$FeSi_2$ film, which is degraded at low temperatures [54].

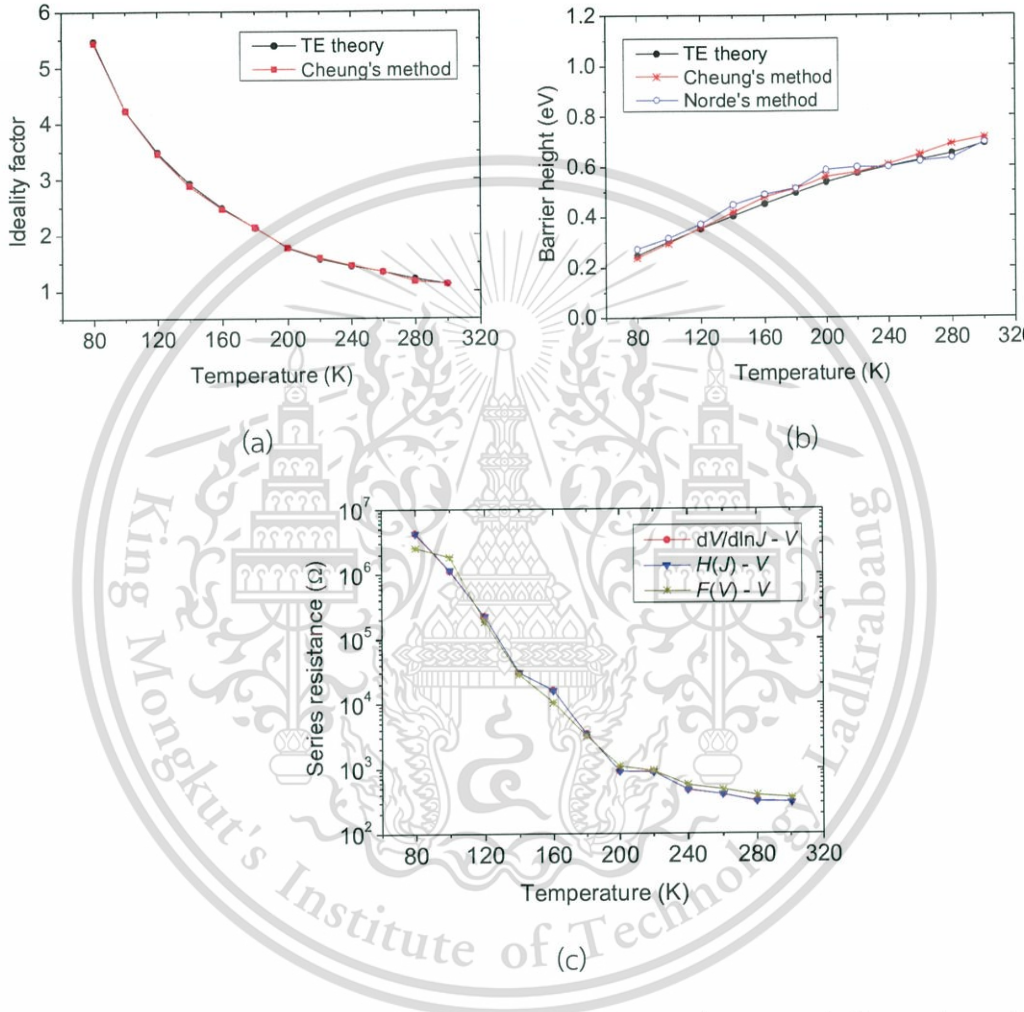

Figure 4.19 (a) Comparison of n values computed by TE theory and Cheung's method, (b) comparison of ϕ_b values obtained using TE theory, Cheung's and Norde's methods, and (c) comparison of R_s values computed by Cheung's and Norde's methods.

Chapter 5
Conclusions

5.1 n-Type β-$FeSi_2$/p-type Si heterojunctions prepared by RFMS

Measurement and analysis were conducted on n-type β-$FeSi_2$/p-type Si heterojunctions grown by RFMS for the dark *J-V* curves as a function of temperature. Their heterojunction parameters were systematically computed using the TE theory, Cheung's method and Norde's method. From computation using the TE theory, the value of n was 1.71 at 300 K and increased to 16.83 at 20 K, whereas the ϕ_b value was 0.59 eV at 300 K and decreased to 0.06 eV at 20 K. The values for both n and ϕ_b were approximately equal to those computed from Cheung's and Norde's methods. The values for R_s computed by Cheung's method were 13.05 Ω at 300 K and 0.14 MΩ at 20 K, which were approximately equal to those computed using Norde's method.

5.2 n-Type NC-$FeSi_2$/p-type Si heterojunctions prepared by PLD

In this work, n-type NC-$FeSi_2$/i-UNCD/a-C/p-type Si heterojunctions were prepared using CAPD and PLD. The dark *J-V* characteristics were measured and analyzed over temperatures ranging between 80-300 K. From these dark *J-V* characteristics, the estimation of junction parameters was carried out using TE theory, Chueng's method and Norde's method. From calculation by TE theory, n value increased and ϕ_b value decreased with decreasing temperature. These parameters for n and ϕ_b were nearly equivalent to those calculated using both Cheung's and Norde's methods. The R_s values calculated by Chueng's method were 300.88 Ω at 300 K and 4.29 MΩ at 80 K. These values were approximately equal to those when using Norde's method.

From the estimation of the junction parameters, the n value was found to be > 1 and ≤ 2 at room temperature. The explanation is that the carrier recombination process was predominant in the carrier transportation mechanism across the heterojunction interface. The existence of defects in β-$FeSi_2$ layer possibly generate deep energy levels in the bandgap, which could behave as recombination centers. For this reason, the weak response of NIR light for application in photodiode of our heterojunctions was likely due to the recombination of photocarriers at the heterojunction interface. Besides, the estimated R_s value at room temperature might be attributed to the diffusion of Fe atoms into the Si side. The diffused Fe atoms

generate deep trap levels in the depletion region, which produced the leakage current in the formed heterojunctions. Also, the NIR light detection was degraded because the photo-generated carriers were trapped in the deep trap levels owing to the diffusion of Fe atoms.

At low temperatures, based on the estimation of the n value, this value increased to be > 2 at low temperatures. This might explain that a tunneling process was dominant the carrier transportation mechanism. This is because of the existence of interface states at the heterojunction interface. This existence would be likely the cause for reducing photocurrent at low temperatures. Besides, the occurrence of spikes in conduction and valence bands owing to a heterojunction band offset were elevated due to the Fermi levels of Si and β-$FeSi_2$ layers approaching the center of the band gaps at low temperatures. These spikes act as a barrier for the photo-generated carriers flowing at the heterojunction interface. In addition, the estimation of the R_s, this parameter increased at low temperatures. This might be attributable to the low mobility of carriers in the β-$FeSi_2$ layers. Generally, the value of R_s for rectifying devices should be small as possible to improve quality of the devices.

References

[1] Sunohara T., Kobayashi K., and Suemasu T. 2006. **"Epitaxial growth and characterization of Si-based light-emitting Si/β-$FeSi_2$ film/Si double heterostructures on Si(001) substrates by molecular beam epitaxy."** Thin Solid Films 508(1-2): 371–375.

[2] Leong D., Harry M., Reeson K. J., and Homewood K. P. 1997. **"A silicon/iron-disilicide light-emitting diode operating at a wavelength of 1.5 μm."** Nature 387(6634): 686–688.

[3] Suemasu T., Ugajin Y., Murase S., Sunohara T., and Suzuno M. 2007. **"Photoluminescence decay time and electroluminescence of p-Si/β-$FeSi_2$ particles/n-Si and p-Si/β-$FeSi_2$ film/n-Si double heterostructures light-emitting diodes grown by molecular beam epitaxy."** Journal of Applied Physics 101(12): 124506-1-124506-6.

[4] Bost M. C., and Mahan J. E. 1988. **"A clarification of the index of refraction of beta-iron disilicide."** Journal of Applied Physics 64(4): 2034–2037.

[5] Promros N., Yamashita K., Iwasaki R., and Yoshitake T. 2012. **"Effects of hydrogen passivation on near-infrared photodetection of n-type β-$FeSi_2$/p-type Si heterojunction photodiodes."** Japanese Journal of Applied Physics 51(10R): 108006-1–108006-2.

[6] Promros N., Yamashita K., Izumi S., Iwasaki R., Shaban M., and Yoshitake T. 2012. **"Near-infrared photodetection of n-type β-$FeSi_2$/intrinsic Si/p-type Si heterojunctions at low temperatures."** Japanese Journal of Applied Physics 51(9S2): 09MF02-1-09MF02-4.

[7] Milosavljević M., Wong L., Lourenço M., Valizadeh R., Colligon J., Shoa G., Homewood K. P. 2010. **"Correlation of structural and optical properties of sputtered $FeSi_2$ thin films."** Japanese Journal of Applied Physics 49(8): 081401-1–081401-4.

[8] Hossain M. Z., Mimura T., Miura N., Uekusa S. 2009. **"Surface morphology and luminescence characterization of β-$FeSi_2$ thin films prepared by pulsed laser deposition."** Applied Surface Science 256(4): 1227–1231.

[9] Promros N., Chen L., Yoshitake T. 2013. **"Near-infrared photodetection in n-type nanocrystalline $FeSi_2$/p-type Si heterojunctions."** J. Nanosci. Nanotechnol. 13: 3577–3581,

[10] Nakamura S., Aoki T., Kittaka T., Hakamata R., Tabuchi H., Kunitsugu S., Takarabe K. 2007. **"Facing target sputtered iron-silicide thin film."** Thin Solid Films 515: 8205–8209.

[11] Promros N, Yamashita K, Li C, Kawai K, Shaban M, Okajima T, Yoshitake T. 2012. **"n-Type nanocrystalline $FeSi_2$/intrinsic Si/p-type Si heterojunction photodiodes fabricated by facing-target direct-current sputtering."** Japanese Journal of Applied Physics 51: 021301-1–021301-4.

[12] Victor E. Borisenko, 2000. **"Semiconducting Silicides."** Springer-Verlag Berlin Heidelberg.

[13] Tatar B., Kutlu K., and Urgen M. 2007. **"Synthesis of β-$FeSi_2$/Si heterojunctions for photovoltaic applications by unbalanced magnetron sputtering."** Thin Solid Films 516(1): 13–16.

[14] Christensen N. E. 1990. **"Electronic structure of β-$FeSi_2$."** Phys. Rev. B 42: 7148-7153.

[15] Eppenga R. 1990. **"Ab Initio band-structure calculation of the semiconductor β-$FeSi_2$."** Journal of Applied Physics 68: 3027-3028.

[16] Yoshitake T., Inokuchi Y., Yuri A., and Nagayama K. 2006. **"Direct epitaxial growth of semiconducting β-$FeSi_2$ thin films on Si(111) by facing targets direct-current sputtering."** Applied physics letters 88: 182104-1-182104-3.

[17] Udono H., Kikuma I., Okuno T., Matsumoto Y., Tajima H., and Komuro S. 2004. **"Optical properties of β-$FeSi_2$ single crystals grown from solutions."** Thin Solid Films 461: 182-187.

[18] Arushanov E., Bucher E., Kloc Ch., Kulikova O., Kulyuk L., and Siminel A. 1995. **"Photoconductivity in n-type β-$FeSi_2$ single crystals."** Phys. Rev. B 52(1): 20-23.

[19] Dimitriadis C. A., Werner J. H., Logothetidis S., Stutzmann M., Weber J., and Nesper R. 1990. **"Electronic properties of semiconducting $FeSi_2$ films."** Journal of Applied Physics 68(4): 1726-1734.

[20] Clark S.J., Al-Allak H.M., Brand S., Abram R.A. 1998. **"Structure and electronic properties of $FeSi_2$."** Phys. Rev. B 58(16): 10389-10393.

[21] Mahan J. E., Geib K. M., Robinson G. Y., Long R. G., Xinghua Y., Bai G., Nicolet M. A., and Nathan M. 1990. **"Epitaxial films of semiconducting $FeSi_2$ on (001) silicon."** Applied Physics Letters 56: 2126-2128.

[22] Mahan J. E., Thanh V. L., Chevrier J., Berbezier I., Derrien J. 1993. **"Surface electron-diffraction patterns of β-$FeSi_2$ films epitaxially grown on silicon."** Journal of Applied Physics 74(3): 1747-1761.

[23] Chewier J., Thanh V. L., Nitschse S., and Derrien J. 1992. **"Epitaxial growth of β-$FeSi_2$ on silicon (111): a real-time RHEED analysis."** Applied Surface Science 56-58: 438-443.

[24] Natoli J. Y., Berbezier I., and Derrien J. 1994. **"Growth of β-$FeSi_2$ on Si(111) by chemical beam epitaxy."** Applied Physics Letters 65(11): 1439-1441.

[25] Ji S.Y., Wang J.F., Lim J. W., Isshiki M. 2006. **"Growth process of β-$FeSi_2$ epitaxial film on Si(111) by molecular beam epitaxy."** Applied Surface Science 253: 444–448.

[26] Terai Y., Hashimoto S., Noda K., and Fujiwara Y. 2009. **"Epitaxial growth of Al-doped β-$FeSi_2$ on Si(111) substrate by reactive deposition epitaxy."** Phys. Status Solidi C 6(6): 1488–1491.

[27] Oostra D. J., BulleLieuwma C. W. T., Vandenhoudt D. E. W., Felten F., and Jans J. C. 1993. **"β-$FeSi_2$ in (111)Si and in (001)Si formed by ion beam synthesis."** Journal of Applied Physics 74(7): 4347-4352.

[28] Shaban M., Nomoto K., Nakashima K., and Yoshitake T. 2008. **"Low temperature annealing of n-type β-$FeSi_2$/p-type Si heterojunctions."** Japanese Journal of Applied Physics 47(5): 3444–3446.

[29] Wunstel K., and Wagner P. 1982. **"Interstitial iron and iron-acceptor pairs in silicon."** Applied Physics A Solids and Surfaces 27(4): 207-212.

[30] Shaban M., Nomoto K., Izumi S., and Yoshitake T. 2009. **"Characterization of near-infrared n-type β-$FeSi_2$/p-type Si heterojunction photodiodes at room temperature."** Applied physics letters 94(22): 222113-1-222113-3.

[31] Promros N., Baba R., Takahara M., Mostafa T. M., Sittimart P., Shaban M., and Yoshitake T. 2016. **"Epitaxial growth of β-$FeSi_2$ thin films on Si(111) substrates by radio frequency magnetron sputtering and their application to near-infrared photodetection."** Japanese Journal of Applied Physics 55: 06HC03-1-06HC03-4.

[32] Milosavljevic´ M., Shao G., Bibic´ N., McKinty C. N., Jeynes C., and Homewood K. P. 2001. **"Amorphous-iron disilicide: A promising semiconductor."** Applied physics letters 79(10): 1438-1440.

[33] Milosavljevi M., Shao G., Lourenço M. A., Gwilliam R. M., Homewood K. P., Edwards S. P., Valizadeh R., and Colligon J. S. 2005. **"Transition from amorphous to crystalline beta phase in co-sputtered $FeSi_2$ films as a function of temperature."** Journal of applied physics 98(12): 123506-1-123506-6.

[34] Yoshitake T., Yatabe M., Itakura M., Kuwano N., Tomokiyo Y., and Nagayama K. 2003. **"Semiconducting nanocrystalline iron disilicide thin films prepared by pulsed-laser ablation."** Applied Physics Letters 83(15): 3057-3059.

[35] Takarabe K., Doi H., Mori Y., Fukui K., Shim Y., Yamamoto N., Yoshitake T., and Nagayama K. 2006. **"Optical properties of nanocrystalline $FeSi_2$ and the effects of hydrogenation."** Applied Physics Letters 88(6): 061911-1-061911-3.

[36] Shaban M., Kondo H., Nakashima K., and Yoshitake T. 2008. **"Electrical and Photovoltaic Properties of n-Type Nanocrystalline-$FeSi_2$/p-Type Si Heterojunctions Prepared by Facing-Targets Direct-Current Sputtering at Room Temperature."** Japanese Journal of Applied Physics 47(7): 5420–5422.

[37] Shaban M., Kawai K., Promros N., and Yoshitake T., 2010. **"n-Type Nanocrystalline-$FeSi_2$/p-Type Si Heterojunction Photodiodes Prepared at Room Temperature."** IEEE Electron Device Letters 31(12): 1428-1430.

[38] Nomoto K., Shaban M., Kondo H., and Yoshitake T. 2008. **"Photovoltaic properties of n-type nanocrystalline-$FeSi_2$/intrinsic-Si/p-type Si heterojunctions fabricated by facing-targets DC sputtering."** Optoelectronic and Microelectronic Materials and Devices COMMAD 2008: 263-266.

[39] Promros N., Baba R., Kishimoto H., Sittimart P., Hanada T., Hanada K., Zkria A., Shaban M., and Yoshitake T. 2016. **"Characterization of n-Type Nanocrystalline Iron Disilicide/Intrinsic Ultrananocrystalline Diamond/Amorphous Carbon Composite/p-Type Silicon Heterojunctions at Low Temperatures."** Journal of Nanoelectronics and Optoelectronics 11: 1-6.

[40] Sze S.M. and Kwok K. Ng. 2007. **"Semiconductor Devices Physics and Technology 3rd ed."** John Wiley & Sons: United States of America.

[41] Shaban M, Nakashima K., Yokoyama W., and Yoshitake T. 2007. **"Photovoltaic Properties of n-type ß-$FeSi_2$/p-type Si Heterojunctions."** Japanese Journal of Applied Physics 46(27): L667–L669.

[42] Shaban M., Izumi S., Nomoto K., and Yoshitake T. 2009. **"n-Type ß-$FeSi_2$/intrinsic-Si/p-type Si heterojunction photodiodes for near-infrared light detection at room temperature."** Applied Physics Letters 95(16): 162102-1-162102-3.

[43] Murphy E. L., and Good JR. R. H. 1956. **"Thermionic Emission, Field Emission, and the Transition Region."** Physical Review 102(6): 1464-1473.

[44] Richardson O. W. 1903. **"The Electrical Conductivity Imparted to a Vacuum by Hot Conductors."** Philosophical Transactions of the Royal Society of London Series A 201: 497-549.

[45] Cheung S. K., and Cheung N. W. 1986. **"Extraction of Schottky diode parameters from forward current voltage characteristics."** Applied Physics Letters 49(2): 85-87.

[46] Norde H. 1979. **"A modified forward I-V plot for Schottky diodes with high series resistance."** Journal of Applied Physics 50(7): 5052-5053.

[47] Aydemir U., Taşçıoğlu İ., Altındal Ş., and Uslu İ. 2013. **"A detailed comparative study on the main electrical parameters of Au/n-Si and Au/PVA:Zn/n-Si Schottky barrier diodes."** Materials Science in Semiconductor Processing 16(6): 1865-1872.

[48] Tuğluoğlu N., Koralay H., Akgül K.B., and Çavdar Ş. 2016. **"Detailed Analysis of Device Parameters by Means of Different Techniques in Schottky Devices."** Journal of Electronic Materials 45(8): 3859-3865.

[49] Farag A. A., Yahia I. S., Wojtowicz T., and Karczewski G. 2010. **"Influence of temperature and illumination on the electrical properties of p-ZnTe/n-CdTe heterojunction grown by molecular beam epitaxy."** Journal of Physics D: Applied Physics 43(21): 215102-1–215102-7.

[50] Caglar M., and Yakuphanoglu F. 2009. **"Fabrication and electrical characterization of flower-like CdO/p-Si heterojunction diode."** Journal of Physics D: Applied Physics 42(4): 045102-1-045102-5.

[51] Kus F. O., Serin T., and Serin N. 2009. **"Current transport mechanisms of n-ZnO/p-CuO heterojunctions."** Journal of Optoelectronics and Advanced Materials 11(11): 1855-1859.

[52] Serin T., G¨urakar S., Serin N., Yıldırım N., and Ozyurt K. F. 2009. **"Current flow mechanism in Cu_2O/p-Si heterojunction prepared by chemical method."** Journal of Physics D: Applied Physics 42(22): 225108-1-225108-5.

[53] Rodrigues A. M. 2008. **"Extraction of Schottky diode parameters from current-voltage data for a chemical-vapor-deposited diamond/silicon structure over a wide temperature range."** Journal of Applied Physics 103(8): 083708-1–083708-6.

[54] Zkria A., Shaban M., Hanada T., Promros N., and Yoshitake T. 2016. **"Current transport mechanisms in n-type ultrananocrystalline diamond/p-type Si heterojunctions."** Journal of Nanoscience and Nanotechnology 16(12): 12749-12753.

[55] Funasaki S., Promros N., Iwasaki R., Takahara M., Shaban M., and Yoshitake T. 2013. **"Fabrication of mesa structural n-type nanocrystalline-$FeSi_2$/p-type Si heterojunction photodiodes by liftoff technique combined with photolithography."** Phys. Status Solidi C 10(12): 1785-1788.

Curriculum Vitae

Name: **First Name:** Phongsaphak

Family Name: SITTIMART

Contact address or 31 Buengboon Sisakaet Province Thailand 33220.

Permanent address: Phone: +6689-624-5844 Email: psittimart@gmail.com

Personal Information: Date of Birth: 12 June 1992

Sex: Male

Marital status: Single

Nationality: Thai

Place of Birth: Nakonrachasima Province, Thailand

Education:

2005-2011: High School Major Mathematical Science, Sisaketwitayalai School (GPA 3.77)

2011-2015: Bachelor Degree, Department of Applied Physics (Alternative Energy), Faculty of Science, King Mongkut's Institute of Technology Ladkrabang (KMITL) (GPA 3.25 with a Second Honor medal)

2015-2017: Master Degree, Department of Applied Physics, Faculty of Science, King Mongkut's Institute of Technology Ladkrabang (KMITL) (GPA 3.62)

English Skill: TOEIC 615

Experiences:

- **Research Assistant (2013-2014):**
  Plasma and Advanced Materials Technology Research Unit, Department of Physics, Faculty of Science, Chulalongkorn University, Bangkok, Thailand.

  Responsibilities
  Preparation and characterization of iron disilicide and heterojunction combined with silicon for photodiode and photovoltaic applications. (Collborative Research Program for Alumni Members 2014 supported by AUN/SEED-Net JICA)

- **Research Assistant (2014-2015):**
  Department of Physics, Faculty of Science, King Mongkut's Institute of Technology Ladkrabang (KMITL), Bangkok, Thailand.
  Responsibilities
  Design and Construction of a Compact DC Magnetron Sputtering Source and Its Characteristics. (supported by KMITL Research Fund)

- **Research Assistant (2016-present):**
  Department of Physics, Faculty of Science, King Mongkut's Institute of Technology Ladkrabang (KMITL), Bangkok, Thailand.
  Responsibilities
  Preparation of Iron disilicide thin film by sputtering and their physical properties. (Collborative Research Program for Alumni Members 2016 supported by AUN/SEED-Net JICA)

- **Teaching Assistant (2012-present):**
  Department of Applied Physics, Faculty of Science, King Mongkut's Institute of Technology Ladkrabang (KMITL).

  Responsibilities
  Intermediate Physics Laboratory 1, 2 (Science Student Groups).

- **Teaching Assistant (2015-present)**

  Department of Applied Physics, Faculty of Science, King Mongkut's Institute of Technology Ladkrabang (KMITL).

  Responsibilities

  General Physics Laboratory Physics 1,2 (Engineering, Science Student Groups).

List of Presentations

1. P. Sittimart, N. Patanoo, S. Pongnitichareom, M. Horprathum, N. Promros, W. Bhuanthunnavin, B. Poawsawutyunyong, The 40th Congress on Science and Technology of Thailand (STT40), P.70, Magnetic Field Characteristics of a Locally Designed Compact Mangnetron Sputtering Source, 2014. (Thailand)

2. N. Promros, P. Sittimart, M. Takahara, T. Hanada, L. Chen, T. Yoshitake, Pacific Rim Symposium on surfaces, Coatings & Interfaces, Electrical Transport Properties and Photodetection Performances of n-Type NC-FeSi2/i-UNCD/a-C/p-Type Si Heterojuction Photodiodes at Low Temperature, December 7-11, 2014. (Kahala Coast Hawaii U.S.A.)

3. N. Promros, P. Sittimart N. Patanoo, M. Horprathum, W. Bhaunthumnavin and B. Paosawatyanyong, AUN/SEED-Net Regional Conference on Materials Engineering, Page 41, Design of Compact Magnetron Sputtering Source for Thin Film Deposition, November 11-12, 2014. (Kuala Lumpur Malaysia)

4. Nathaporn Promros, Phongsaphak Sittimart, Nattatip Patanoo, Sukrit Kongnithichalerm, Mati Horprathum, Worawan Bhathumnavin, and Boonchoat Paosawatyanyong, The 2nd International Conference on Applied Physics and Material Applications, Physical Properties of Copper Films Deposited by Compact-Size Magnetron Sputtering Source with Changing Magnetic Field Strength, May 28-30, 2015. (Thailand)

5. Nathaporn Promros, Nattarat Hongsa, Dalin Pakjakun, Nattanee Suthayanun, Phongsaphak Sittimart, Kenji Hanada, Motoki Takahara, T.Hanada, R.Baba, Tarek M. Mostafa, Li Chen and Tsuyoshi Yoshitake, The 2nd International Conference on Applied Physics and Material Applications, Characterization of Dioade Parameters at Low Temperatures in n-Type Nanocrytalline Iron

Disilicide/Intrinsic Ultrananocrystalline Diamond/Amorphous Carbon Composite/p-Type Silicon Heterojuctions, May 28-30, 2015. (Thailand)

6. Nathaporn Promros, Ryuji Baba, Motoki Takahara, Tarek M. Mostafa, Phongsaphak Sittimart, Mahmoud Shaban, and Tsuyoshi Yoshitake, Epitaxial Growth of β-$FeSi_2$ Thin Films on Si(111) Substrates by Radio Frequency Magnetron Sputtering and Their Application to Near-Infrared Photodetection, Proceedings of International Symposium on Dry Process, November 5-6, 2015 (2015). (Japan)

7. Nathaporn Promros, Phongsaphak Sittimart, Ryuji Baba, Hirokazu Kishimoto, Takanori Hanada, Abdelrahman Zkria, Mahmoud Shaban, and Tsuyoshi Yoshitake, International Conference on Small Science, Phuket Thailand, Investigation of Electrical Transport Properties in Heterojunctions Comprising Silicon Substrate and Nanocrystalline Iron Disilicide Films, November 4-7, 2015. (Phuket, Thailand).

8. Phongsaphak Sittimart, Adison Nopparuchikun and Nathaporn Promros, The 42nd Congress on Science and Technology of Thailand (STT42), Junction parameters of n-type β-$Fesi_2$/p-type Si heterojunctions fabricated using radio frequency magnetron sputtering, November 30 - December 2, 2016 (Thailand).

9. Asanlaya Duangrawa, Phongsaphak Sittimart, Adison Nopparuchikun, Peeradon Onsee, Sakmongkon Teakchaicum, and Nathaporn Promros, Estimation of density of interface state in n-Type Nanocrystalline $FeSi_2$/ p-Type Si Heterojunctions Fabricated by using Facing-Target Direct-Current Sputtering" STT42, 2016 (Thailand).

10. Peeradon Onsee, Asanlaya Duangrawa, Sakmongkon Teakchaicum, Phongsaphak Sittimart, Adison Nopparuchikun, and Nathaporn Promros, Estimation of interface state density in n-type nanocrystalline $FeSi_2$/intrinsic Si/p-type Si heterojunctions by utilizing Hill-Coleman method, APAC, 2016. (Japan)

11. Phongsaphak Sittimart, Adison Nopparuchikun, Peeradon Onsee, Asanlaya Duangrawa, Sakmongkon Teakchaicum, and Nathaporn Promros, The 5th Thailand International Nanotechnology Conference, **Characterization of junction parameters in n-type nanocrystalline iron disilicide/intrinsic ultrananocrystalline diamond/amorphous carbon composite/p-type silicon heterojunctions**, November 27-29, 2016 (Thailand).

12. Phongsaphak Sittimart, Asanlaya Duangrawa, Peeradon Onsee, Sakmongkon Teakchaicum, Adison Nopparuchikun, and Nathaporn Promros, The 14th International Conference on Nano Science and Nano Technology 2016 (ICNST 2016), ***I-V, C-V-f* and *G-V-f* Characteristic Curves of Heterojunctions Comprising n-Type Nanocrystalline Iron Disilicide Films and p-Type Silicon Substrate,** November 10-11, 2016 (South Korea).

13. Adison Nopparuchikun, Nathaporn Promros, Sakmongkon Teakchaicum, Peeradon Onsee, Asanlaya Duangrawa, Phongsaphak Sittimart, Hirokazu Kishimoto, Tomohiro Nogami, and Tsuyoshi Yoshitake, ***C-V-f* and *G-V-f* Characteristics of n-Type ß-FeSi2/p-Type Si Heterojunctions Fabricated by Using Radio Frequency Magnetron Sputtering**, Proceedings of International Symposium on Dry Process, 2016 (Japan).

14. Sakmongkon Teekchaicum, Nnathaporn Promros, Phongsaphak Sittimart and Boonchoat Paosawatyanyong, The International Conference on Applied Physics and Materials Application (ICAPMA 2017), **Surface Morphology and Hydrophobic Property of Diamond-Like Carbon Films Deposited Using Magnetron Sputtering Source by Changing Outer Magnets,** 31 May-2 June, (2017). (Thailand)

List of Publications

1. Phongsaphak Sittimart, Asanlaya Duangrawa, Peeradon Onsee, Sakmongkon Teakchaicum, Adison Nopparuchikun, Nathaporn Promros. 2017. **Interface State Density and Series Resistance of n-Type Nanocrystalline $FeSi_2$/p-Type Si Heterojunctions Formed by Utilizing Facing-Target Direct-Current Sputtering.** Journal of Nanoscience and Nanotechnology: Accepted (waiting for online publishing) (Impact=1.383).

2. Phongsaphak Sittimart, Adison Nopparuchikun, Peeradon Onsee, Asanlaya Duangrawa, Sakmongkon Teakchaicum, and Nathaporn Promros. 2017. Characterization of junction parameters in n-type nanocrystalline iron disilicide/intrinsic ultrananocrystalline diamond/amorphous carbon composite/p-type silicon heterojunctions. Materials Today: Proceedings: Accepted (waiting for online publishing).

3. Adison Nopparuchikun, Nathaporn Promros, Sakmongkon Teakchaicum, Peeradon Onsee, Asanlaya Duangrawa and Phongsaphak Sittimart. 2017. Carrier Transportation Properties and Series Resistance of n-Type ß-$Fesi_2$/p-Type Si Heterojunctions Fabricated by RF Magnetron Sputtering. Japanese Journal of Applied Physics 56 (2017) 06HE06-1-06HE06-5. (Impact=1.122)

4. Phongsaphak Sittimart, Adison Nopparuchikun and Nathaporn Promros. 2017. Computation of Heterojunction Parameters at Low Temperatures in Heterojunctions Comprised of n-Type ß-$FeSi_2$ Thin Films and p-Type Si(111) Substrates Grown by Radio Frequency Magnetron Sputtering. Advances in Materials Science and Engineering 2017 (2017) 6590606-1-6590606-8. (Impact=1.299)

5. Phongsaphak Sittimart, Adison Nopparuchikun and Nathaporn Promros, Junction parameters of n-type ß-$FeSi_2$/p-type Si heterojunctions fabricated using radio frequency magnetron sputtering, Proceeding of The 42nd Congress on Science and Technology of Thailand (STT 42), B1_098 (2016) pp. 11-16.

6. Asanlaya Duangrawa, Peeradon Onsee, Sakmongkon Teakchaicum, Phongsaphak Sittimart, Adison, Nopparuchikun, Nathaporn Promros, Estimation of density of interface state in n-type nanocrystalline $FeSi_2$/p-type Si heterojunctions fabricated by using facing-target direct-current sputtering, Proceeding of the 42nd Congress on Science and Technology of Thailand (STT 42), B1_137 (2016) pp. 25-29.

7. Promros N., Baba R., Takahara M., Mostafa T. M., Sittimart P., Shaban M., and Yoshitake T. 2016. Epitaxial growth of ß-$FeSi_2$ thin films on Si(111) substrates by radio frequency magnetron sputtering and their application to near-infrared photodetection. Japanese Journal of Applied Physics 55 (2016) 06HC03-1-06HC03-4. (Impact=1.122)

8. Promros N., Baba R., Kishimoto H., Sittimart P., Hanada T., Hanada K., Zkria A., Shaban M., and Yoshitake T. 2016. Characterization of n-Type Nanocrystalline Iron Disilicide/Intrinsic Ultrananocrystalline Diamond/Amorphous Carbon Composite/p-Type Silicon Heterojunctions at Low Temperatures. Journal of Nanoelectronics and Optoelectronics 11 (2016) 1-6. (Impact=0.675)

9. Nathaporn Promros, Phongsaphak Sittimart and Weerasaruth Kaenrai. 2016. Investigation of Electrical Transport Properties in Heterojunctions Comprised of Silicon Substrate and Nanocrystalline Iron Disilicide Films. Int. J. Nanotechnol. 13 (2016) 903-912. (Impact=0.502)

10. Nathaporn Promros, Phongsaphak Sittimart, Nattatip Patanoo, Sukrit Kongnithichalerm, Mati Horprathum, Worawan Bhathumnavin, and Boonchoat Paosawatyanyong. 2016. Physical Properties of Copper Films Deposited by Compact-Size Magnetron Sputtering Source with Changing Magnetic Field Strength, Key Engineering Materials 675-676 (2016) 193-196.

11. Nathaporn Promros, Kenji Hanada, Motoki Takahara, Takanori Hanada, Ryuji Baba, Phongsaphak Sittimart, Li Chen and Tsuyoshi Yoshitake. 2015. Characterization of n-Type Nanocrystalline iron Disilicide/Intrinsic Ultrananocrystalline Diamond/Amorphous Carbon Composite/p-Type Silicon Heterojunction Photodiodes. Advanced Materials Research 1131 (2016) 20-24.

12. Nathaporn Promros, Dalin Prajakkan, Nantharat Hongsa, Nattanee Suthayanan, Phongsaphak Sittimart, Motoki Takahara, Ryuji Baba, Tarek M. Mostafa, Mahmoud Shaban, and Tsuyoshi Yoshitake. 2015. Temperature Dependent Current-Voltage Characteristics of n-Type ß-$FeSi_2$/Intrinsic Si/p-Type Si Heterojunctions, Advanced Materials Research. 1120-1121 (2015) 435-439.

13. Sakmongkon Teakchaicum, Peeradon Onsee, Asanlaya Duangrawa, Phongsaphak Sittimart, and Nathaporn Promros, Estimation of Interface State Density of n-Type Nanocrystalline FeSi2/p-Type Si Heterojunctions in Mesa Structure Fabricated by Utilizing Photolithography, Proceedings of The 41St National and 5th International Graduate Research Conference Poster Presentation (Science/Agriculture/Environment and Technology), (2016) pp. 30-37.

Internship

Yoshitake Laboratory, Department of Electrical and Material Science, Kyushu University, Japan
(Period: 29 July – 27 August 2014) (Scholarship supported by JICA)

Plasma and Advanced Materials Technology Research Laboratory (PAMT), Department of Physics, Faculty of Science, Chulalongkorn University, Thailand
(Period: 1 May – 31 May 2014)

Reference Person

Asst. Prof. Dr. Nathaporn Promros
Phone +6686-379-8648 E-mail nathaporn_promros@kyudai.jp

Asst. Prof. Dr. Boonchoat Poasawatyanyong
Phone +6681-816-9127 Email paosawat@sc.chula.ac.th